NOVA SCHOOL OF SCIENCE & TECHNOLOGY

DEPARTAMENT OF MATERIALS SCIENCE

Nuno Filipe Glória Marques

Master of science in
Micro and Nanotechnologies Engineering

High efficiency planar-type perovskite solar cells using SnO_2 composite as an electron transport layer

Msc Micro and Nanotechnologies Engineering

NOVA University Lisbon

October, 2023

DEPARTAMENT OF MATERIALS SCIENCE

High efficiency planar-type perovskite solar cells using SnO_2 composite as an electron transport layer

Nuno Filipe Glória Marques

Msc Micro and Nanotechnologies Engineering

Adviser: Dr. Shrabani Panigrahi
Pos-Doc Fellow
Faculty of Sciences and Technology – NOVA University of Lisbon

Co-advisers: Dr. Hugo Manuel Brito Águas
Associate Professor
School of Sciences and Technology – NOVA University of Lisbon

Examination Committee:

Chair: Prof. Rodrigo Ferrão de Paiva Martins,
Full Professor, Faculty of Sciences and Technology – NOVA University of Lisbon

Rapporteurs: Dr Raquel Cristina Teixeira Maricato,
Pos-Doc Fellow, Faculty of Sciences and Technology – NOVA University of Lisbon

Adviser: Dr. Shrabani Panigrahi,
Pos-Doc Fellow, Faculty of Sciences and Technology – NOVA University of Lisbon

Members: Professor Hugo Manuel Brito Águas,
Associate Professor, Faculty of Sciences and Technology – NOVA University of Lisbon

MASTER IN MICRO AND NANOTECNOLOGY ENGINEERING

NOVA University Lisbon
October, 2023

ACKNOWLEDGMENTS

Com a etapa escolar mais importante da minha vida terminada não posso deixar de agradecer às pessoas que a tornaram possível e as que me mais contribuíram para o seu sucesso.

Em primeiro lugar, gostaria de agradecer ao Professor Rodrigo Martins e à Professora Elvira Fortunato por me garantirem as condições de trabalho necessárias para a realização da minha dissertação, graças às ótimas instalações e equipamento, tanto no CENIMAT como no CEMOP.

Em seguida gostaria de agradecer aos meus orientadores, a Dra. Shrabani Panigrahi e Professor Hugo Águas pela confiança em mim depositada e pela oportunidade que me deram de estudar na área das Perovskites que considero bastante interessante e importante para o futuro da área fotovoltaica. *A very special thanks must be given to my adviser Dr. Shrabani Panigrahi for all the patience and trust deposited in me. Also, for the massive amount of help and feedback that you give me. Due to external factors, this thesis was much harder and exhausting to do but you always kept pushing me forward so without you this work wouldn't be possible. Thank you.*

Por último, gostaria de agradecer à minha família por me ter apoiado nesta etapa difícil e decisiva da minha vida académica, em especial aos meus pais e à minha irmã pela paciência e esforço que tiveram para comigo a assim ajudar a tornar isto possível. Obrigado!

ABSTRACT

Perovskite solar cells (PSCs) have become one of the most promising and exciting photovoltaic technology due to their simplicity in fabrication, amazing optoelectronic properties of the perovskites, and high-power conversion efficiency. Perovskites possess extraordinary optoelectronic properties such as high carrier mobility, long diffusion length, long charge carrier lifetime, high absorption coefficient and tunable bandgap. The electron transport layer (ETL) in PSCs plays a significant role in the charge carrier dynamics and photovoltaic characteristics of devices. In this study, Ethylenediaminetetraacetic acid (EDTA)-complexed SnO_2 (E-SnO_2) was effectively prepared by using a simple, ambient-conditioned, low temperature chemical synthesis technique and used as an ETL for PSCs to increase the device efficiency and long-term stability. Different concentration-based E-SnO_2 solution was prepared by mixing EDTA solution with various concentrations of SnO_2 aqueous solutions to optimize the best concentration for high efficiency PSCs. It has been observed that EDTA can improve the properties of the perovskite layer by increasing the grain size, crystallinity, and surface potential, facilitating the carrier transport from the perovskite to HTL. After EDTA treatment, lead iodide (PbI_2) was also appeared across the GBs and surfaces of the perovskite film which has been utilized to passivate the defects at perovskite film surfaces. According to the literature, the Fermi level of E-SnO_2 is better matched with the conduction band of perovskite resulting in a higher open-circuit voltage (V_{OC}). An enhancement of V_{OC} ~ 200 mV mainly causes for the efficiency improvement from 13.20 % to 15.51 % for the best E-SnO_2 (7.5%) based solar cell. The utilization of the complex ETL technique demonstrates the significant potential of E-SnO_2 as an ETL in regulating the perovskite layer and hence, enhancing the stability and efficiency of PSCs.

Keywords: Perovskite solar cell, Electron transport layer, SnO_2, E-SnO_2, lead iodide

RESUMO

As células solares de perovskite (PSCs) tornaram-se uma das tecnologias fotovoltaicas mais promissoras e interessantes devido à sua simplicidade de fabrico, incríveis propriedades optoelectrónicas e alta eficiência de conversão de energia. As perovskites possuem propriedades optoelectrónicas extraordinárias, como alta mobilidade de portadores, longo comprimento de difusão, longa vida útil do portador de carga, alto coeficiente de absorção e bandgap ajustável. A camada de transportadora de eletrões (ETL) em PSCs desempenha um papel significativo na dinâmica do portador de carga e nas características fotovoltaicas dos dispositivos. Neste estudo, ácido etilenodiaminotetracético (EDTA) complexado com SnO_2 (E-SnO_2) foi efetivamente preparado usando uma técnica de síntese química simples, condicionada ao ambiente e de baixa temperatura e foi usado como um ETL para PSCs para aumentar a eficiência do dispositivo e estabilidade a longo prazo. Diferentes concentrações de soluções de E-SnO_2 foram preparadas misturando solução de EDTA com várias concentrações de soluções aquosas de SnO_2 para otimizar a melhor concentração para PSCs de alta eficiência. Foi observado que o EDTA pode melhorar as propriedades da camada de perovskite, aumentando o tamanho do grão, a cristalinidade e o potencial de superfície, facilitando o transporte de portadores da perovskite para o HTL. Após o tratamento com EDTA, iodeto de chumbo (PbI_2) também apareceu nos GBs e nas superfícies do filme de perovskite, o qual foi utilizado para passivar os defeitos nas superfícies do filme de perovskite. De acordo com a literatura, o nível de Fermi de E-SnO_2 combina melhor com a banda de condução da perovskite, resultando em uma maior tensão de circuito aberto (V_{OC}). Um aumento de V_{OC} ~ 200 mV causa principalmente a melhoria da eficiência de 13.20% para 15.51% para a melhor célula solar baseada em E-SnO_2 (7.5%). A utilização da técnica complexa de ETL demonstra o potencial significativo do E-SnO_2 como ETL na regulação da camada de perovskite e, portanto, no aumento da estabilidade e eficiência das PSCs.

Palavras chave: Células solares de perovskite, camada transportadora de eletrões, SnO_2, E-SnO_2, iodeto de chumbo

CONTENTS

LIST OF FIGURES

LIST OF TABLES

ACRONYMS

4-tBP	4-tert-Butylpyridine
AFM	Atomic Force Microscopy
CIGS	Copper indium gallium selenide
CIS	Copper Indium Selenide
CPD	Contact potential difference
CZTS	Copper zinc tin sulfide
DMF	N,N-dimethylformamide
DMSO	Dimethyl Sulfoxide
DSSC	Dye-sensitized solar cell
EDTA	Ethylene diamine tetraacetic acid
EQE	External quantum efficiency
ETL	Electron Transport Layer
FF	Fill factor
FIB	Focused ion beam
HTL	Hole Transport Layer
I_{SC}	Short-Circuit Current
ITO	Indium tin oxide
J_{SC}	Short-Circuit Current Density
KPFM	Kelvin probe force microscopy
LiTFSI	Bis(trifluoromethane)sulfonimide lithium salt
MA	Methylammonium
MAI	Methylammonium Iodide
$MAPbI_3$	Methylammonium Lead Iodide
Pb	Lead
PbI_2	Lead iodide
PCE	Power Conversion Efficiency
PL	Photoluminescence
PSC	Perovskite Solar Cells
PV	Photovoltaic
SEM	Scanning Electron Microscopy
SnO_2	Tin dioxide
Spiro-OMETAD	2,2',7,7'-tetrakis(N,N-di-p-meth-oxyphenylamine)-9',9'-spirobifluorene
TCO	Transparent Conducting Oxide
TiO_2	Titanium dioxide

UPS	Ultraviolet Photoelectron spectroscopy
UV	Ultraviolet
UV-Vis	Ultraviolet-Visible
V_{OC}	Open-circuit voltage
XPS	X-ray photoelectron spectroscopy
XRD	X-Ray Diffraction
ZnO	Zinc oxide

SYMBOLS

°C	Degrees Celsius
µL	Microliter
µm	Micrometer
Au	Gold
cm	Centimeter
Eg	Optical bandgap
eV	Electron volt
h	Hour
mA	Milliampere
mg	Milligram
min	Minute
mm	Millimeter
mV	Millivolts
nm	Nanometer
pA	Picoampere
Rpm	Rotations per minute
s	Second
V	Volts
λ	Wavelength
Ω	Ohms

1

INTRODUCTION

The annual energy consumption and the number of environmental and health problems related to the use of fossil fuels are both rising as a result of the rapid increase in the global population [1]. These problems sparked people's attention to new clean and renewable energy sources [2]. In recent years, Photovoltaic (PV) technologies have been the most studied alternative to fossil fuels and the most practical solution for the long-term sustainability of the human species. Nowadays, Silicon solar cells are the most used and developed type of solar cells, but, due to their complicated and costly manufacturing process and low theoretical limit of power conversion efficiency (PCE) of 33%, new PV technologies are coming on the scene as an alternative [3].

Photovoltaic technologies can be divided into three generations. The first generation based by crystalline silicon-based cells that can be polycrystalline or monocrystalline. Despite being first generation, these types of solar cells still represent around 95% of PV market. The second generation is based on thin film solar cells which are cheaper to produce than the silicon solar cells. The second generation of solar cells uses thin film materials like amorphous silicon, CIS, CIGS and CdTe [4]. The third generation, also known as emerging photovoltaics, is the semiconducting-based solution-processed solar cells which includes organic photovoltaics (OPVs), copper zinc tin sulfide (CZTS), dye-sensitized solar cells (DSSCs), quantum dot solar cells, and perovskite solar cells (PSCs) [5].

PSCs have drawn a lot of interest due to its exceptional optical properties, inexpensive material components and easily developed by low temperature synthesis technique. The potential of PSCs in the field of photovoltaics is demonstrated by the significant increase in power conversion efficiency (PCE) from 3.8% to over 26% within past few years, as shown in Figure 1, achieved by using different composition of perovskites as an absorber and interface engineering in solar cells [6]. Despite these properties, PSCs need improvements related to its stability, upscaling, and better choice of materials to become viable for commercialization [7].

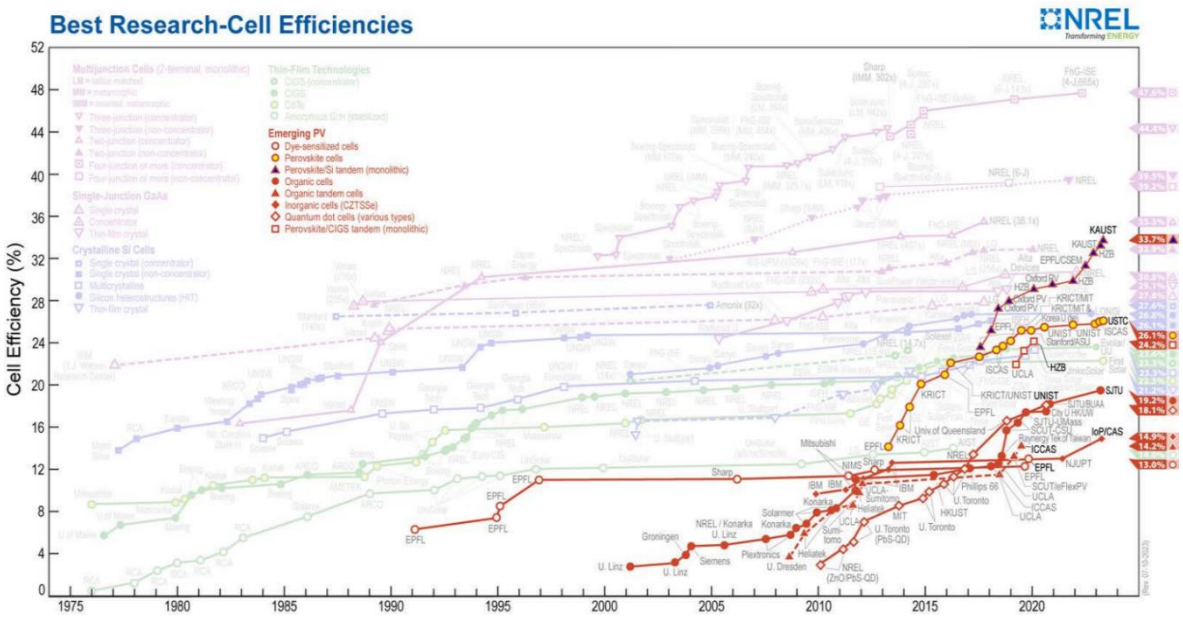

Figure 1 - Adapted plot of the evolution of the best recorded efficiency of all types of solar cell technologies with the emerging photovoltaic technologies highlighted in red [8].

1.1 Perovskite

1.1.1 Crystal structure of perovskites

Perovskites have been known since 1839, when Gustav Rose found them for the first time in the Russian Ural Mountains [9]. The term perovskite came from a calcium titanium oxide mineral ($CaTiO_3$) and nowadays is used to describe the cubic crystal structure of the ionic compound ABX_3 [10]. Since its discovery, new derivatives of perovskites structure have been developed and studied but they don't see much use in solar cells due to its still low PCE [11].

In the general formula of perovskites ABX_3 shown in Figure 2, where "A" is a larger size cation that occupies the corners of the cubic structure, "B" is a smaller metal cation that occupies the center of the unitary cell and X represents the small halide anion that resides in the center of the faces of the unitary cell [12]. For the organic cation in position "A" is normally used methylammonium ($CH_3NH_3^+$ or MA) or formamidinium ($NH_2CH{=}NH_2^+$ or FA), for the B metal cation is used a divalent metal cation such as Sn^{2+}, Pb^{2+} and Ge^{2+}, and for the X halogen is normally used Cl^-, Br^- and I^- [13].

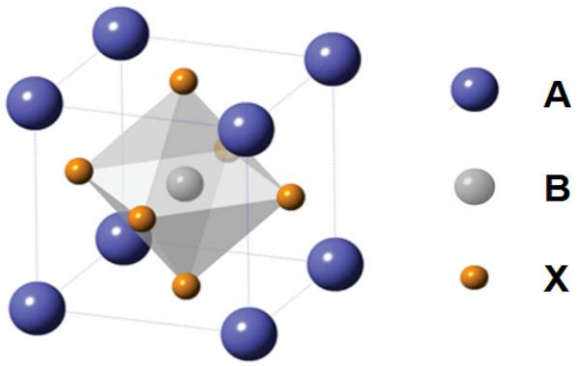

Figure 2 -ABX_3 structure of a cubic perovskite [14].

The formation and stability of the perovskite can be determined the Goldschmidt's formula which allows to calculate the tolerance factor (t) through the atomic radii,

$$t = \frac{R_A + R_X}{\sqrt{2}(R_B + R_X)}$$

where R_A, R_B and R_X are the ionic radii of the ions A, B and X ions, respectively. Generally, a 3D perovskite structure can be formed in the range of $0.8<t<1.1$. These 3D structures can be deformed if $0.8<t<0.9$ or they can be cubic if $0.9<t<1$ [15]. Another parameter used to calculate the formability and stability of the perovskite structures is the octahedral factor (μ) that is used to predict if the cation on the B site fits into the X_6 octahedral structure. The octahedral factor can be expressed as:

$$\mu = \frac{R_B}{R_X}$$

To achieve a stable perovskite structure, the octahedral factor value should be between 0.442 and 0.895 [16].

1.1.2 Perovskite properties

In the last few years, organic inorganic lead halide PSCs commonly methylammonium lead iodide ($MAPbI_3$) PSCs have attracted more attention due to their most promising PCE. The high PCE of PSCs originates from their correlative inherent material properties such as perfect band gap of halide perovskites, high threshold absorption cross section, defect tolerant feature, long carrier diffusion length, low exciton binding energy etc.[17]–[19] .These remarkable properties associated with economical solution processability make them excellent candidates for the next-generation photovoltaic solar cells technologies [20]. The high absorption of this material makes the use of a thinner absorber layer possible and consequently the carries will have to travel smaller distances before they are collected and therefore, reducing the non-radiative recombination [21]. Despite the attractive potentials of the lead halide PSCs, challenges are yet remaining in their approach for substantial commercial applications. The first issue is the very short-term device stability especially when the issue is exposed to heat and humidity [22]. The second and main issue is the presence of heavy metal like “Lead (Pb)” in these perovskite materials. The toxicity of lead is one of the key challenges that must be overcome [23].

1.2 Architecture of Perovskite Solar Cells

The basic planar structure of PSCs usually consist five main layers which are the transparent conductive oxide (TCO) deposited over a glass substrate, an n-type layer called electron transport layer (ETL) that serves to facilitate the transport of electron photogenerated by the light absorbed by the perovskite, the perovskite absorber layer or intrinsic layer responsible for absorbing light and producing current, an p-type layer called hole transport layer (HTL) which serves to conduct the holes photogenerated in the perovskite, and the metal electrode [24].

In terms of architecture, PSCs can be classified as mesoscopic type if they possess a thick mesoporous metal oxide material or as planar type if they have a compact layer as an ETL, as shown in Figure 3 (a). The planar type PSCs can be sub classified into "standard architecture" (negative-intrinsic-positive, NIP-type) and "inverted architecture" (positive-intrinsic-negative, PIN-type). This subclassification of the PSCs depends on the deposition of the sequence of the layers [25].

The standard n-i-p configuration consists of a substrate coated with a transparent conducting oxide (TCO) where the ETL is deposited first followed by the perovskite, then the HTL and finally the deposition of the metallic top electrode as shown in Figure 3 (b). Figure 3 (c) shows the inverted p-i-n configuration that starts with TCO where the HTL is deposited, then the perovskite, followed by the ETL and lastly the metal electrode on top. Both configurations have their advantages and disadvantages, and the choice of configuration will determine the applications and the efficiency of the cell. The n-i-p configuration is more used since it allows a more flexible choice of materials, reduced hysteresis, better charge extraction and can be made by easy processing technique [26].

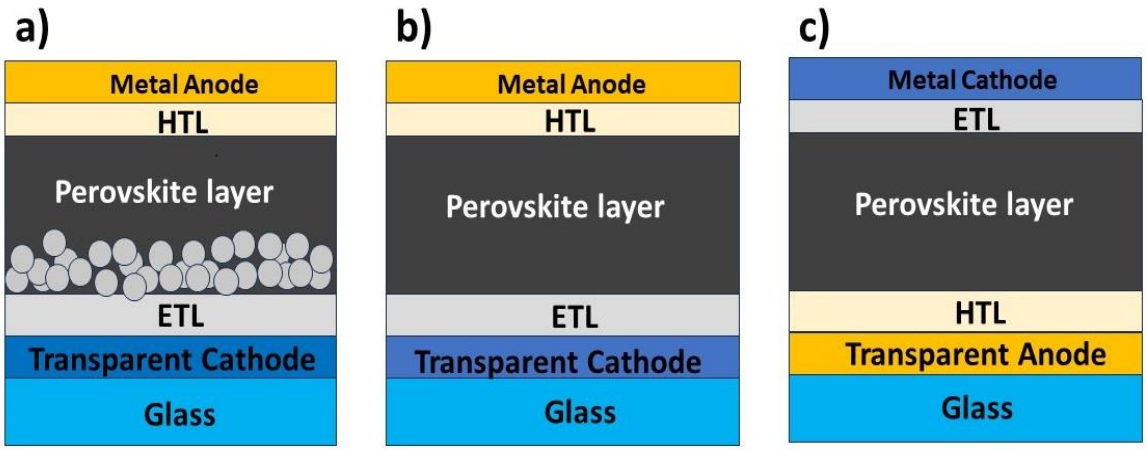

Figure 3 - Device structure of a) mesoscopic, b) n-i-p planar, c) p-i-n planar perovskite solar cell. Adapted from [27].

1.3 Electron Transport layer

ETL is a wide bandgap n-type semiconductor that has a big impact on the charge carriers dynamics and photovoltaic performance of the PSCs. A good optical transmittance of ETL ensures that enough light enters the perovskite absorber, a well-matched energy level with the perovskite materials provides the desired open-circuit voltage (V_{OC}), and a high electron mobility effectively removes carriers from the active layer to prevent charge recombination, among other fundamental requirements [24]. It is the layer that is in between the perovskite layer and the transparent conducting electrode layer [27]. This layer is used to extract the electrons from the photogenerated electron-hole pairs and transport them to the conducting electrode [28], which suppress recombination [29].

Titanium dioxide (TiO_2) is the most widely used ETL in PSCs because this ETL tend to have the highest efficiencies in PSCs [27]. However, TiO_2 suffers from low electron mobility (around 10^{-5} cm^2. V^{-1} .s^{-1}) [30], a high density of surface defects and high temperature deposition process [31].

Zinc oxide (ZnO) is another probable ETL that has a considerable potential to be the replacement of TiO_2. This material has some advantages such as low-temperature processing, high bulk electron mobility (between 205 and 300 cm^2. V^{-1} .s^{-1}) and high conductivity. However, it possesses a massive drawback being the fact that it can easily react with the perovskite film when the annealing temperature is above 100 °C which affects the long-term stability of the solar cell [32]. To attain its full potential, the material must be exposed to UV-light with the same energy as the ZnO bandgap [33].

1.3.1 SnO_2

SnO_2 is also a preferable promising candidate as an ETL for highly efficient PSCs compared to the more conventional TiO_2 because of its low temperature processing technique, higher transmittance, larger bandgap (3.6–4.5 eV), superior optical and electrical properties, better band alignment with perovskite, and exceptional stability in the presence of moisture, heat, and light with negligible photoactivity [34]. The lower conduction band, higher carrier mobility (240 $cm^2/(V.s)$) and high conductivity causes a reduction in nonradiative recombination [35]. The fact is that SnO_2 has a wide bandgap together with a refractive index <2 which makes SnO_2 coatings deposited on glass have a high transmittance of approximately 89%, allowing light to pass through and be absorbed by the perovskite layer. It also has a very high UV stability because it doesn't absorb much UV light due to its wide bandgap [36]. SnO_2 has high chemical stability due to being less hygroscopic [37] and can be processed at low temperature using simple processes like sol-gel making it viable for large scale commercialization [38].

1.3.2 Why E-SnO_2?

Even though SnO_2 currently possesses amazing qualities, researchers are always exploring for ways to enhance its performance as an ETL. Some of these methods are doping, treatments involving surface passivation, use of two layers with different ETL materials and the use of nanocomposites [31].

Ethylene diamine tetraacetic acid (EDTA) is a substituted diamine. It is a strong chelating agent for metal oxides and a very stable molecule. [39]. This molecule can be complexed with SnO_2 forming E-SnO_2. Theoretically, E-SnO_2 has some advantages over SnO_2, for example, it reduces hysteresis due to the removal of the charge that is usually present between the perovskite/ETL interface, it has higher electron mobility and promotes the growth quality of the perovskite film due to an increase in its grain size [40]. E-SnO_2 has a higher Fermi level which is better matched with the conduction band of the $MAPbI_3$ film which leads to an increase in V_{OC}. In the present work, E-SnO_2 is made using a simple low-temperature method and then used as an ETL in PSCs.

2

MATERIALS AND METHODS

2.1 Device Fabrication

This chapter describes the step-by-step development procedures for PSCs. The production process starts with the substrate preparation which was indium-doped tin oxide (ITO), followed by the ETL, active layer and HTL deposition via spin-coating technique and gold contact deposition via thermal evaporation. All the depositions were performed outside the glove box, in ambient atmosphere with an average value of humidity of 30 %.

2.1.1 Substrate preparation

The unetched ITO coated glass substrates were cut into squares with dimensions of 2.5 × 2.5 cm^2 and then cleaned in an ultrasonic bath. The cleaning process was done with water and detergent, followed by deionized water, acetone, and isopropanol in the respective order. All the baths were performed at a temperature of 60ºC and for 15 minutes each. The substates were dried using an air blow gun and then 3 mm of Kapton tape was set on one side of the substrate to cover the ITO substrate to take one contact from ITO substrate. At last, the substrates were exposed to a 15-minute UV-ozone treatment at 60 °C to eliminate moisture and any remaining residues.

2.1.2 ETL, absorber layer and HTL deposition

For the ETL deposition on the ITO substrate, two different spin-coating techniques were used for two different ETLs. For the SnO_2 layer deposition, 200 µL of aqueous transparent solution of SnO_2 was spin-coated at 4000 rpm for 30 s followed by a heat treatment at 150 °C for 15 min and then annealed at 180 °C for 60 min using a hot plate. For the E-SnO_2 layer deposition, 200 µL of solution was spin-coated at 5000 rpm for 60 s and then dried for 30 min at 60 °C in a vacuum oven to remove the solvent [40].

Before perovskite deposition, ETL-coated substrates were subjected to a UV-ozone treatment for 15 minutes at 150 ° C. For perovskite solution, at first, PbI_2 (215 mg) were dissolved in a mixture of DMF and DMSO at 75°C and then MAI (622 mg) was added in this mixture and followed by constant stirring for 24 hrs. The perovskite solution was deposited via spin coating and the amount of perovskite solution was 100 µL for each sample. The deposition of chlorobenzene serves to help starting the crystallization process and remove the solvent from the perovskite. After annealing, 40 µL of HTL solution was deposited using spin coating technique at 4000 rpm for 30 s. The Spiro-MeOTAD solution was prepared by dissolving 54.2 mg of Spiro-MeOTAD in 0.75 ml of chlorobenzene. The LiTFSI stock solution (520 mg of LiTFSI in 1 ml of acetonitrile) and 21.37 µl of 4-tBP were also added to the solution as additives. For the top electrodes' deposition, gold contacts were deposited using an electron-beam evaporation under high vacuum.

2.1.3 Evaporation of electrode

The samples were placed in a masked holder for the substrates to only get evaporated metal on the wanted surface area that was 2×5 mm^2 and then placed in the electron beam evaporator. The evaporation metal was gold (Au). One pellet of Au resulted in approximately 80 nm thick layer.

2.2 Characterization

2.2.1 Structural and micro-structural characterization.

X-ray Diffraction (XRD). The characterization of the crystal structures of the ETLs and Perovskite layers was done by XRD using a PANalytical X'Pert Pro X-ray diffractometer in Bragg-Brentano geometry, with a monochromatic Cu-Kα (λ=1.5406 Å) radiation source.

Scanning electron microscopy (SEM). The morphological characterizations of the ETLs and the perovskite layers were done with the help of SEM analysis (Carl Zeiss AURIGA Cross Beam workstation). Cross-sectional images of the solar cells were obtained using 30 kV Ga^+ ions at 20 pA and a standard ET type secondary electron detector.

Atomic Force Microscopy (AFM). The surface of the films was characterized using MFP-3D Infinity atomic force microscope from Oxford Instruments Asylum Research (Santa Barbara, CA).
KPFM was used to measure the surface potential. KPFM was performed using Olympus AC240TM probes in an Asylum Research MFP-3D standalone system with the following parameters: 2 N/m spring constant, 70 kHz resonant frequency, and 3 V AC tip voltage in double pass mode.

2.2.2 Optical Characterizations

UV-VIS-NIR spectrophotometry. UV-VIS-NIR spectrophotometer (Shimadzu UV 3101PC with an ISR-260 integrating sphere in a wavelength range of 400-840 nm) is used to observe the absorption and transmission spectra of the samples.

Photoluminescence (PL) spectra was obtained using a high-resolution spectrometer (Horiba Jobin Yvon, Model: iHR 320) together with a photomultiplier tube.

2.2.3 X-ray photoelectron spectroscopy (XPS)

XPS measurements were performed using an AXIS Supra+ spectrometer by Kratos Analytical with 300 W X-ray power and monochromatic Al K α radiation where a pass energy is 40 eV.

2.2.4 Electrical characterization

The forward bias current density-voltage (*J-V*) tests were carried out using a workstation (Sciencetech SS1.6kW-A-2-Q system with Keithley source meter: Model 2400) under AM1.5 G (1 sun conditions, 100 $mW.cm^{-2}$). External quantum efficiency (EQE) measurement was carried out by a Xenon lamp (Newport) attached to a monochromator (Newport).

3

RESULTS AND DISCUSSION

The main objective of this work is to explore the benefits of modifying the SnO_2 ETL by complexing it with EDTA and analyze which concentration of SnO_2/E-SnO_2 is optimal for device fabrication. All the solutions were prepared and deposited in ambient conditions, outside the glove box. The best results for each concentration are reported in this chapter.

Preparation of ETL solutions

In order to study the concentration-dependent effects of the SnO_2 and E-SnO_2, the ETL solutions were prepared, characterized, and developed their corresponding devices. In the present thesis, I have mentioned different percentage based SnO_2 and E-SnO_2 ETLs like SnO_2/E-SnO_2 (15%), SnO_2/E-SnO_2 (10%) and so on. The SnO_2 solution with a particular percentage was prepared by diluting the commercial 15% SnO_2 colloidal dispersion from Alfa Aesar with deionized water until the perfect concentration desired. The corresponding E-SnO_2 solution was obtained by mixing that particular concentration of SnO_2 solution with EDTA solution in a 1:1 volume ratio. Table 1 shows the information summary about the concentration of the prepared solutions.

Table 1 – SnO_2 and E-SnO_2 solution preparation with different concentrations.

ETL	Concentration	SnO_2	Deionized H_2O	EDTA
SnO_2	15 wt%	1 mL	-	-
	10 wt%	1 mL	0.5 mL	-
	7.5 wt%	1 mL	1 mL	-
	2.5 wt%	1 mL	5 mL	-
E-SnO_2	15 wt%	1 mL	-	1 mL
	10 wt%	1 mL	0.5 mL	1.5 mL
	7.5 wt%	1 mL	1 mL	2 mL
	2.5 wt%	1 mL	5 mL	6 mL

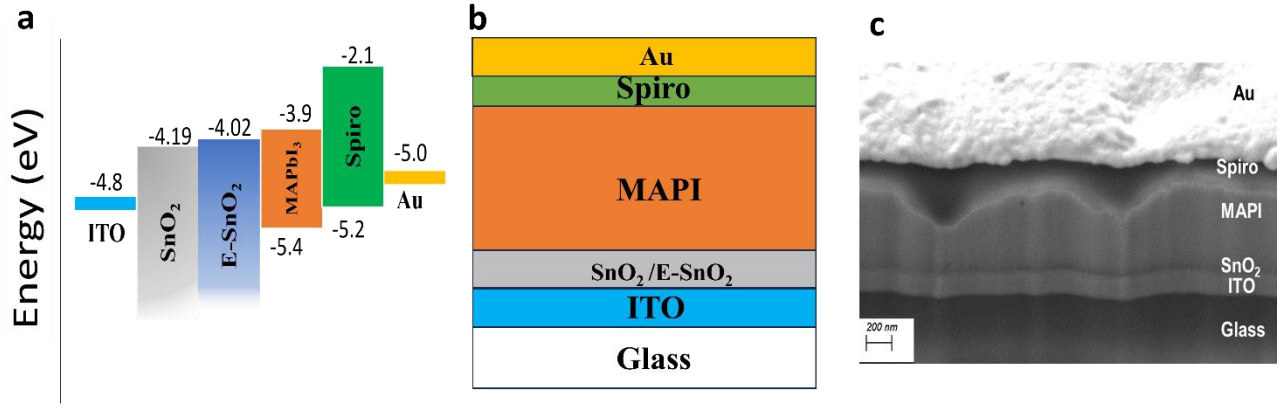

Figure 4 - a) Diagram of the energy levels of the layers of the PSCs [40]. b) Schematic diagram of the produced solar cells. c) Cross-sectional SEM image of the fabricated solar cell.

3.1 For SnO_2 and E-SnO_2 (15%) based ETL

3.1.1 Electrical Characterization of the solar cells

PSCs with 15% concentration of SnO_2 and E-SnO_2 based ETLs were fabricated by applying step-by-step experimental techniques which is already described in chapter 2.1. Figure 5 (a-d) shows the box chart of the best performing solar cells parameters for this particular concentration. The devices based on E-SnO_2 ETL have an higher average V_{OC} and also higher Jsc value than the control sample. Obviously, the efficiency for E-SnO_2 based cells are also higher than the only SnO_2 based PSCs. Among them the parameters for the best solar cell are described below.

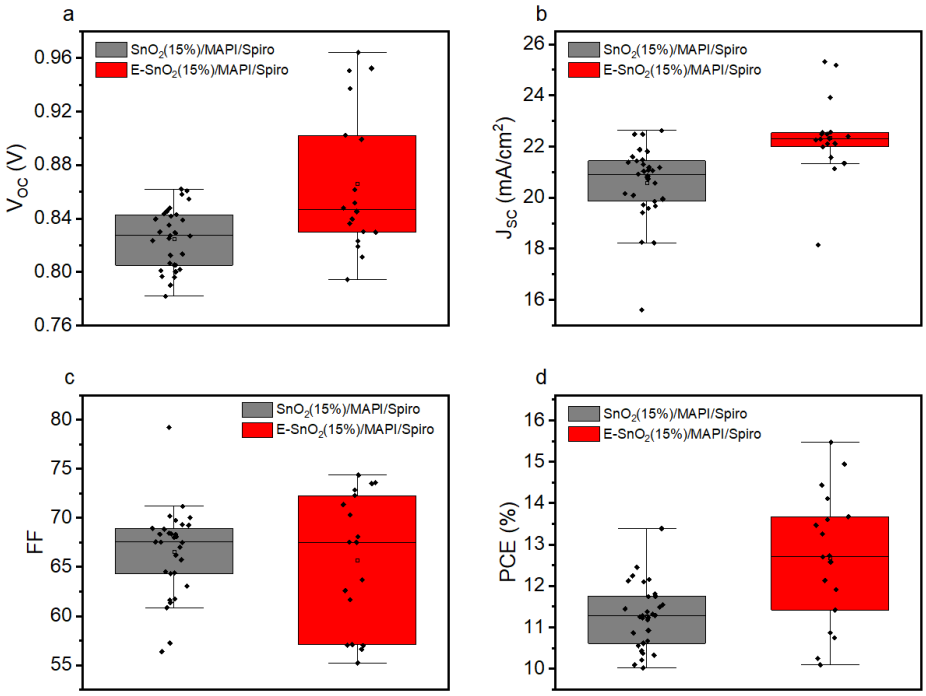

Figure 5 - (a) V_{OC}, (b) J_{SC}, (c) FF and (d) PCE distributions of PSCs with SnO_2 (15%) and E-SnO_2 (15%) based ETLs.

3.1.2 *J-V* curve for best solar cell

Figure 6 (a) shows the *J-V* curve for the best performing cell for 15% SnO_2 and E-SnO_2 based ETLs. The best device for SnO_2 based ETL shows PCE of 13.39% with the value of Jsc=22.63 mA/cm^2, V_{OC}=0.85 V and FF=69.25. On the other hand, the E-SnO_2 ETL based device shows a PCE of 15.47% with the value of J_{SC}=21.58 mA/cm^2, V_{oc}=0.96 V and FF=74.36. Figure 6 (b) shows the EQE spectra for the corresponding cells. From the EQE spectra, the J_{SC} value can be obtained through the following equation:

$$J_{SC} = q\int_{\lambda min}^{\lambda max} \Phi(\lambda) * EQE(\lambda) * d\lambda \quad (1)$$

where q is the elementary charge, Φ is the photon flux and EQE is the external quantum efficiency at wavelength, λ [41]. The value obtained for J_{SC} from the EQE spectra was 20.89 mA/cm^2 for the device with SnO_2 and 20.56 mA/cm^2 for the device with E-SnO_2.

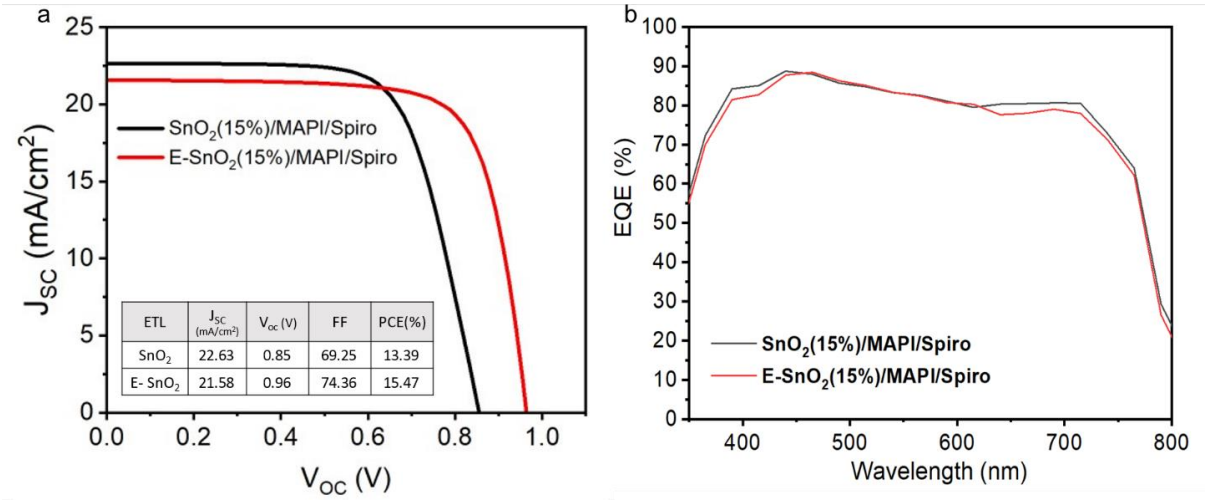

Figure 6 – a) *J-V* curves of the best performing devices based on SnO_2 (15%) and E-SnO_2 (15%) ETLs. b) EQE spectra for those PSCs.

3.1.3 ETL characterization

3.1.3.1 Optical Characterization

UV-Vis spectrophotometry was used to analyze the optical properties of the different ETL layers. Figure 7 (a) shows the optical transmission spectra for SnO_2 (15%) and E-SnO_2 (15%) films deposited on ITO. E-SnO_2 demonstrates a higher transmission at higher wavelengths, however, both samples show good optical properties with transmission values over 80% across visible region which suggest a low parasitical optical loss [42]. Both SnO_2 and E-SnO_2 samples show a sharp decrease in transmission at wavelengths around 300 nm which corresponds to the energy threshold for band edge absorption of SnO_2 [43]. Figure 7 (b) shows the bandgaps of each ETL which were calculated using the Tauc plots. The absorption coefficient (α) and Tauc plots were obtained using equation (2) and (3), respectively,

$$\alpha = -\frac{1}{d}\ln(T) \quad (2)$$

$$(\alpha h\nu) = C(h\nu - Eg)^n \quad (3)$$

Where, d is the thickness of the film, T corresponds to the transmission value (%), hν the photon energy, C is a constant and, Eg the bandgap energy which is 1/2 for allowed direct transitions, 3/2 for forbidden direct

transitions and 2 for indirect transitions. The value of the thickness of the films was measured using the ImageJ software from the cross-sectional SEM image shown in Figure 4 (c) and the value was around 30 nm for both ETLs. The values of thickness for ETLs were also confirmed by the profilometer instrument. The calculated bandgaps for the SnO_2 and E-SnO_2 were 4.12 and 4.13 eV, respectively, which are within the range of SnO_2 bandgap (~3.6 to 4.5 eV) [42]. The large optical bandgap together with the high transmittance demonstrated by the films are preferred features for ETLs, since it allows more photons to travel through the film without being absorbed [44].

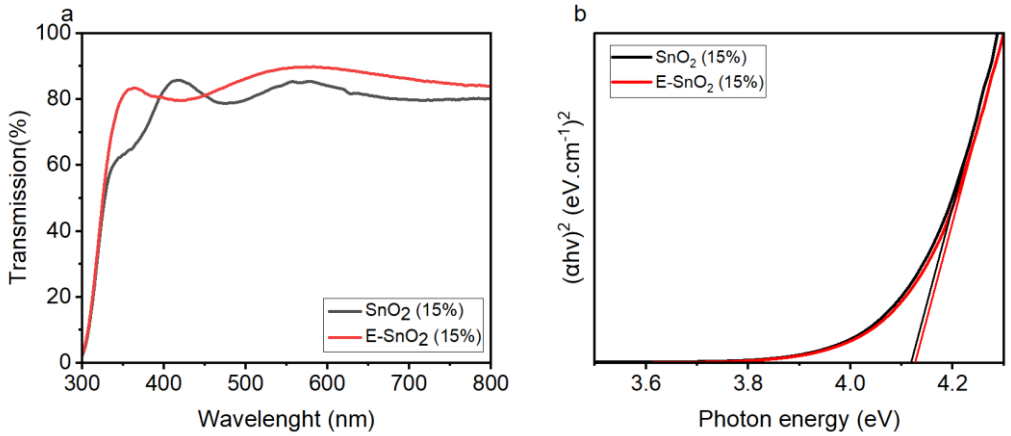

Figure 7 – a) Transmission plot of SnO_2 (15%) and E-SnO_2 (15%) samples. b) Tauc plot (with slope) of the same samples.

3.1.3.2 Structural Characterization

To obtain insights about the SnO_2 and E-SnO_2 films, structural characterization using X-ray diffraction (XRD) analysis was performed. Figure 8 shows the XRD pattern for the (a) SnO_2 and (b) E-SnO_2 films, respectively. By analyzing Figure 8 (a), it's possible to see the presence of (110), (101) and (211) planes, at a 2θ angle of 26.7°, 33.9° and 51.78°, respectively. The predominant peak is the one associated with the orientation (110) plane which corresponds to the minimal surface energy at which SnO_2 crystallizes [45] In Figure 8 (b) there is no prominent peak for SnO_2 which suggest that the E-SnO_2 film is less crystalline. This lack of intense peaks in the XRD pattern of both ETLs might be associated with the low temperature of the annealing process that the samples were subjected (180 and 60°C).

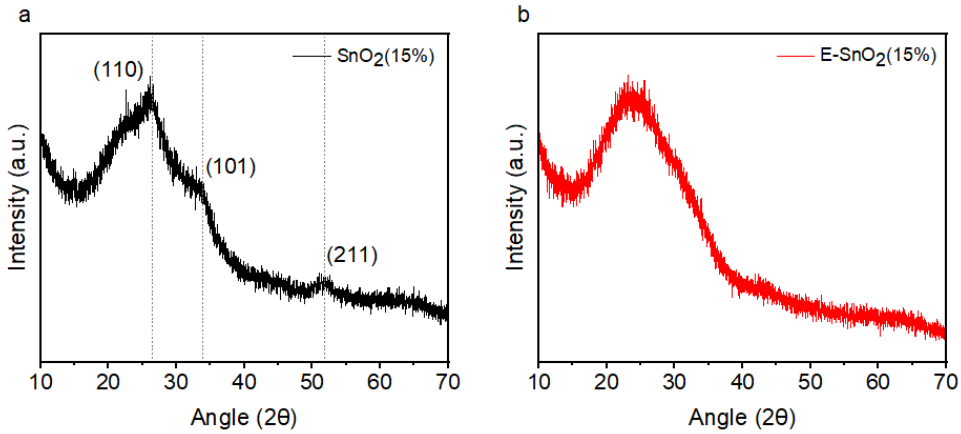

Figure 8 - X-ray diffraction pattern of the a) SnO_2 (15%) and b) E-SnO_2 (15%) thin film.

The top-view scanning electron microscopy (SEM) characterization was performed in order to obtain information about the morphology of the SnO_2 films deposited on ITO. Figure 9 shows the top-view SEM image which show a flat, uniform, and smooth film. For E-SnO_2, it was not possible to take the SEM images for all concentrations because the sample created a charging effect at the time of imaging due to EDTA.

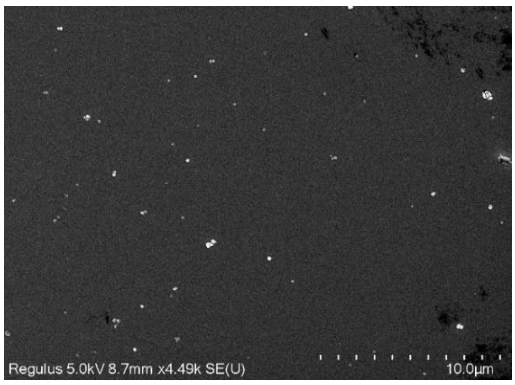

Figure 9 - Scanning electron microscope (SEM) image of SnO_2 (15%) thin film.

3.1.4 Perovskite characterization

3.1.4.1 Optical characterization

The UV-visible absorbance spectra for $MAPbI_3$ films deposited on SnO_2 (15%) and E-SnO_2 (15%) ETLs are shown in Figure 10 (a). Figure 10 (b) shows the corresponding Tauc Plots for these absorbance spectra. The absorbance spectra show that $MAPbI_3$ film deposited on E-SnO_2 has a higher absorbance than SnO_2 in the visible wavelength range from 400 to 800 nm. The band gaps for the perovskites have been calculated in the same way as for the ETLs using the equations (2) and (3). The thickness of the perovskite layer (d) (with ETL) was 500 nm, and it was measured from the cross-sectional FIB-SEM image with the aid of ImageJ software. Since $MAPbI_3$ is a direct band gap semiconductor, it was assigned n=1/2 and the equation become the following:

$$(\alpha hv) = C(hv - Eg)^{\frac{1}{2}} \tag{4}$$

The bandgap value obtained for both perovskite films on SnO_2 and E-SnO_2 ETLs was 1.59 eV which is in line with the values presented in the literature (1.5 to 1.6 eV) [46] .The recombination kinetics of the perovskite films deposited on SnO_2 and E-SnO_2 ETLs has been observed by steady-state photoluminescence (PL) analysis shown in Figure 10 (c). Under an excitation wavelength of 400 nm, both films exhibit an emission peak near 780 nm, which is the result of radiative recombination from the perovskite bandgap. The perovskite film on E-SnO_2 showed slightly weaker PL demonstrating that carriers are extracted more efficiently.

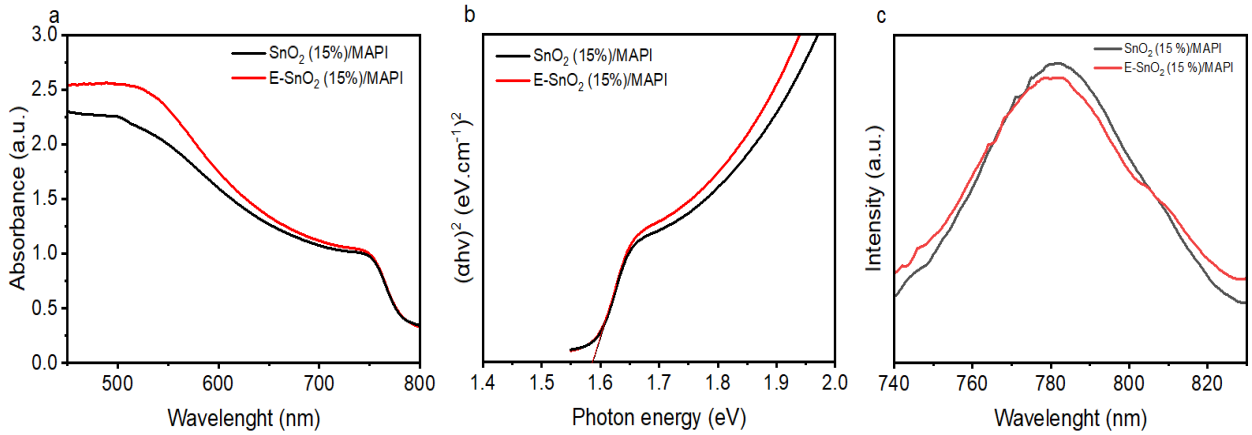

Figure 10 - a) UV–Vis absorption spectra, b) Tauc plot and c) PL spectra of the $MAPbI_3$ films deposited on SnO_2 (15%) and E-SnO_2 (15%) ETLS.

3.1.4.2 Structural characterization

To know about the crystalline structure of the perovskite films, XRD analysis was performed. Figure 11 (a) and (b) show the characteristic peaks of the $MAPbI_3$ film deposited on SnO_2 and E-SnO_2 ETLs. The dominant diffraction peaks that reside at the angle 2θ = 14.09°, 19.92°, 23.52°, 24.44°, 28.42°, 31.79°, 35.1°, 40.43°and 43.1° correspond to the (110), (112), (211), (202), (220), (222), (312), (224), (314) lattice planes of the $MAPbI_3$ tetragonal structure [47].

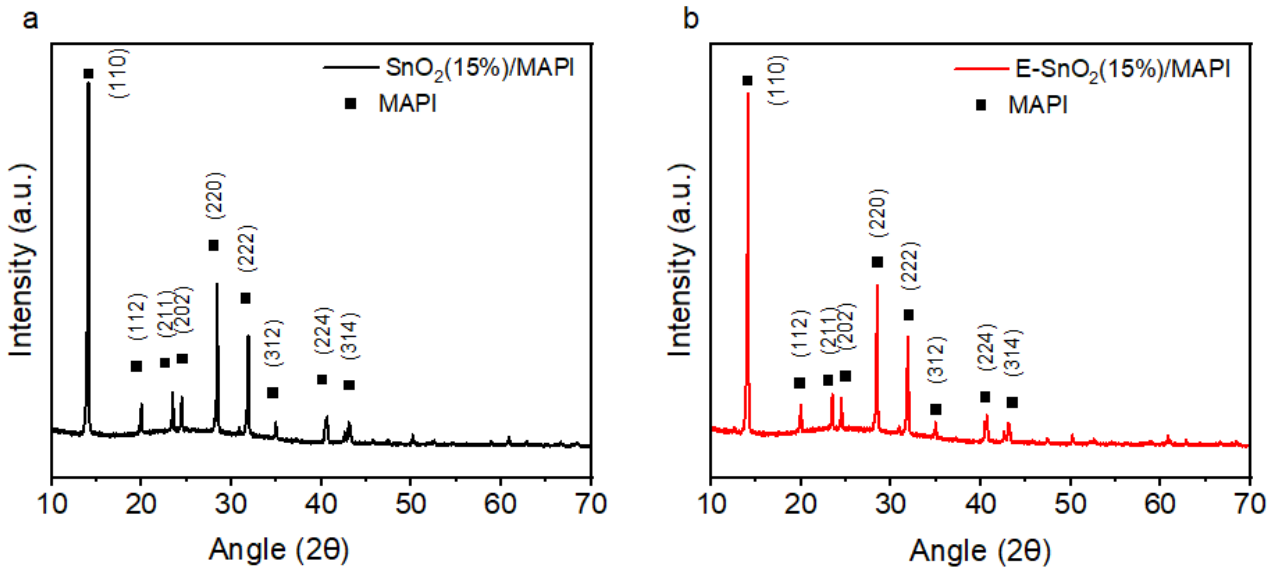

Figure 11 - X-ray diffraction (XRD) spectra of the $MAPbI_3$ films deposited on a) SnO_2 (15%) and b) E-SnO_2 (15%) ETLs.

The surface morphology of the perovskite films was analyzed using SEM. Figure 12 (a) and (b) show the top-view SEM images of the perovskite films deposited on SnO_2 (15%) and E-SnO_2 (15%) ETLs, respectively. Perovskite film on SnO_2 shows average grains, with a round shape but large number of pinholes in-between the grains. Figure 12 (b) shows the perovskite film deposited on E-SnO_2 with bigger size grains and smaller number of pinholes than that for SnO_2. The box plot for the grain size distribution of the perovskite films deposited on both ETLs is represented in Figure 12 (c) and its demonstrates that the perovskite deposited on E-SnO_2 has a larger average grain size which is around 0.98 µm while SnO_2 has an average grain size of 0.86 µm.

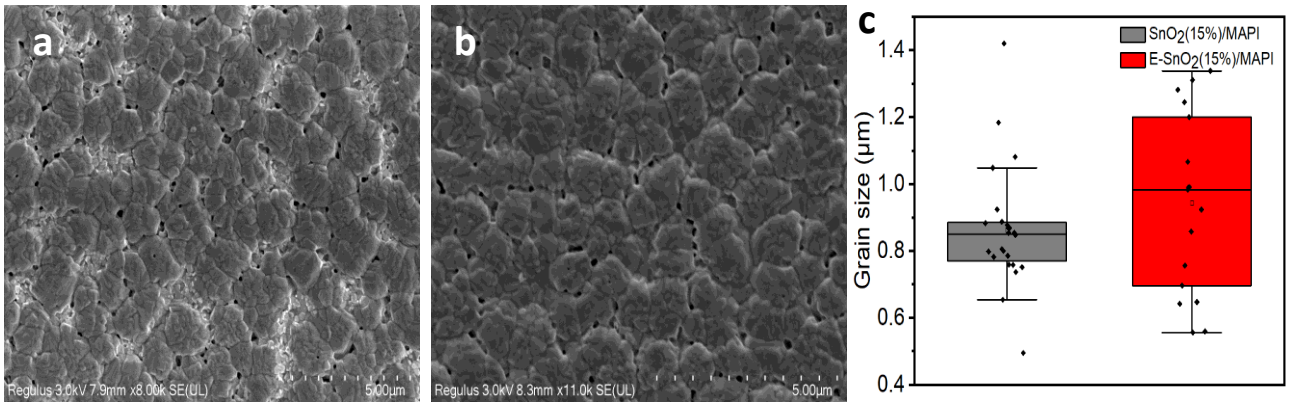

Figure 12 - Top-view SEM images of $MAPbI_3$ films on a) SnO_2 (15%) and b) E-SnO_2 (15%). c) Grain size distribution of the $MAPbI_3$ films.

3.2 For SnO_2 and E-SnO_2 (10%) based ETL

3.2.1 Electrical Characterization of the solar cells

PSCs with 10% concentration of SnO_2 and E-SnO_2 based ETLs were fabricated in the same way which is already described in chapter 2.1. Figure 13 (a-d) shows the box chart of the best performing solar cells parameters. The devices based on E-SnO_2 ETL have average higher V_{OC} but lower Jsc value than the SnO_2 ones. The efficiency for E-SnO_2 based cells are higher than the only SnO_2 based cells due to higher V_{OC} and FF. The parameters for the best cells are described below.

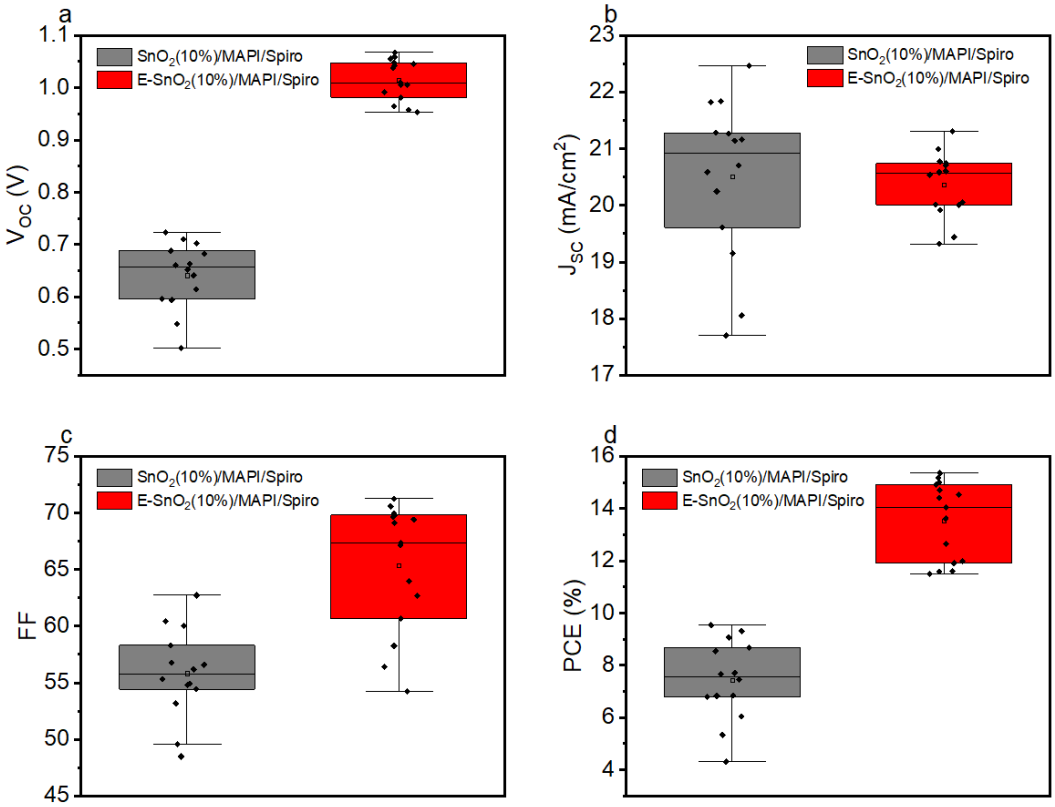

Figure 13 - (a) V_{OC}, (b) J_{SC}, (c) FF and (d) PCE distributions of PSCs with SnO_2 (10%) and E-SnO_2 (10%) based ETLs.

3.2.1 *J-V* curve for the best solar cell

Figure 14 (a) shows the *J-V* curves of the best performing cells for 10% SnO_2 and E-SnO_2 based ETLs, respectively. The best device for SnO_2 based ETL shows PCE of 9.53% where Jsc=21.82 mA/cm^2, V_{OC}=0.72 V and FF=60.43. On the other hand, the E-SnO_2 ETL based device shows a PCE of 15.35% with the value of J_{SC}=20.77 mA/cm^2, V_{oc}=1.06 V and FF=69.79. Figure 14 (b) shows the EQE spectra for the corresponding devices. From the EQE spectra, the obtained J_{SC} values were 20.45 mA/cm^2 and 19.61 mA/cm^2 for the devices with SnO_2 and E-SnO_2 ETLs, respectively.

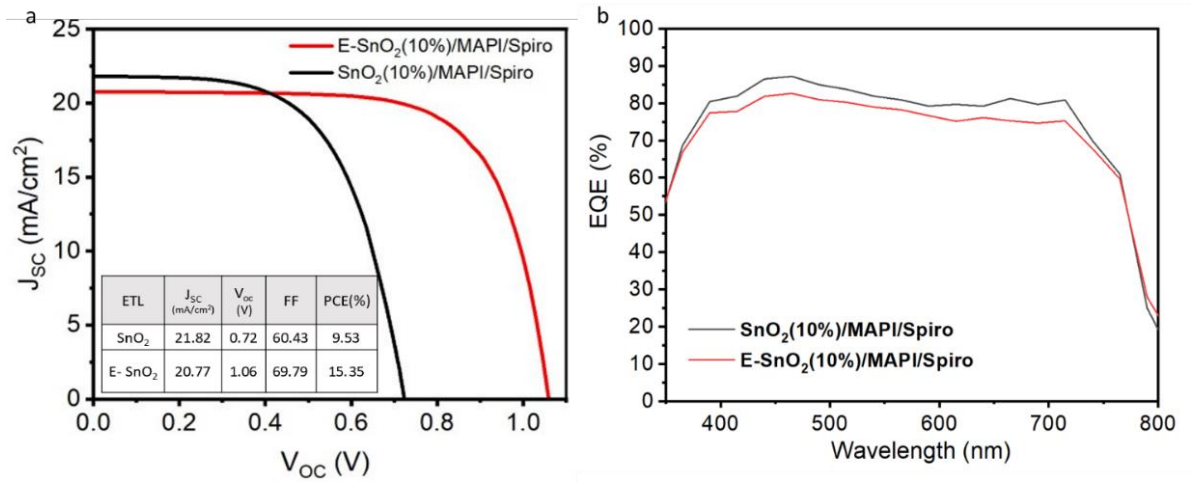

Figure 14 – a) *J-V* curves of the best performing devices based on SnO_2 (10%) and E-SnO_2 (10%). b) EQE spectra for those PSCs.

3.2.2 ETL characterization

3.2.2.1 Optical characterization

UV-Vis spectrophotometry was used to analyze the optical properties of the different ETL layers. Figure 15 (a) shows the transmission spectra for SnO_2 (10%) and E-SnO_2 (10%) films deposited on ITO. E-SnO_2 demonstrates a higher transmission than SnO_2 at wavelengths higher than 500 nm. Both samples show good optical properties with transmission values over 80% across visible region. Figure 15 (b) shows the bandgaps of each ETL which were calculated from the Tauc plots. The calculated bandgaps for the SnO_2 and E-SnO_2 were 4.11 and 4.08 eV, respectively.

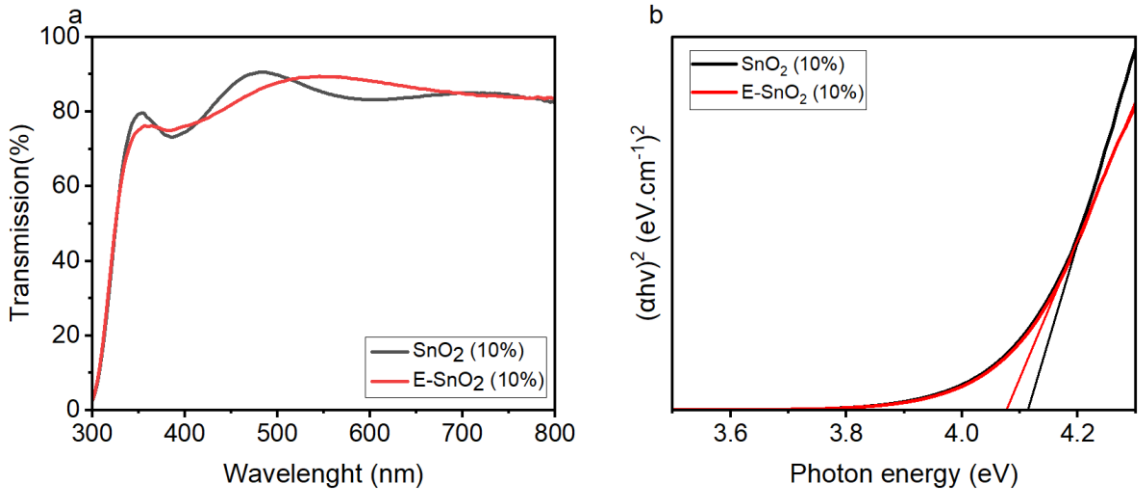

Figure 15 – a) Transmission plot for SnO_2 (10%) and E-SnO_2 (10%) films. b) Tauc plot (with slope) of the same samples.

3.2.2.2 Structural characterization

To obtain insights about the SnO_2 and E-SnO_2 films, structural characterization was performed. Figure 16 shows the XRD pattern for the (a) SnO_2 and (b) E-SnO_2 films, respectively. By analyzing Figure 16 (a), it is possible to see the presence of (110), (101) and (211) planes, at a 2θ angle of 26.7°, 33.9° and 51.78°, respectively. However, these peaks are not very intense which indicates that there was only a partial crystallization of the SnO_2. After EDTA treatment, only one peak (110) is prominent and other peaks intensity decreases (Figure 16 b) indicating a less crystalline ETL.

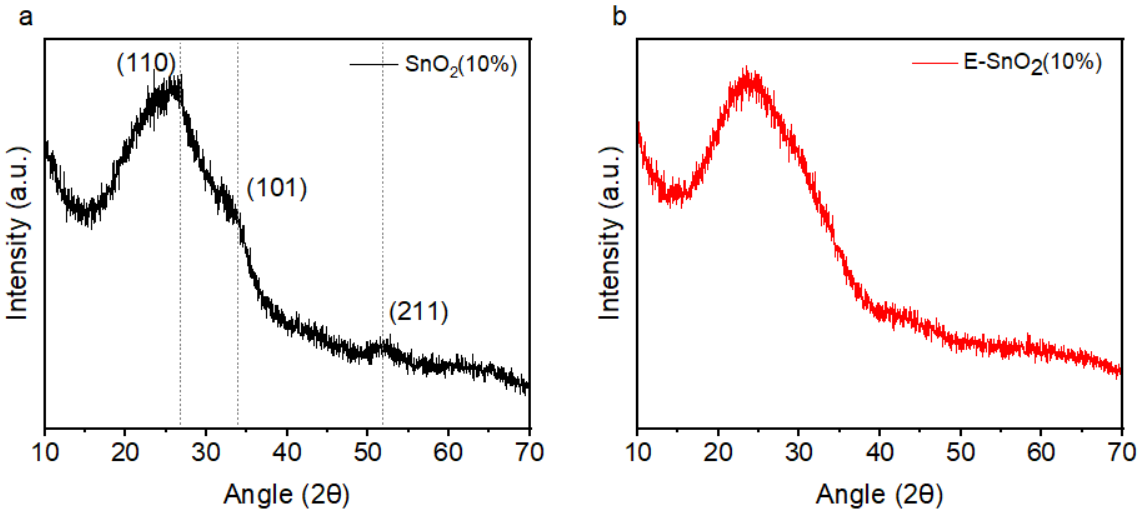

Figure 16 - X-ray diffraction pattern of the a) SnO_2 (10%) and b) E-SnO_2 (10%) thin film.

The top-view SEM characterization was performed in order to obtain information about the morphology of the SnO_2 films deposited on ITO. Figure 17 shows a top-view SEM image of a flat, uniform, and smooth film with no defects.

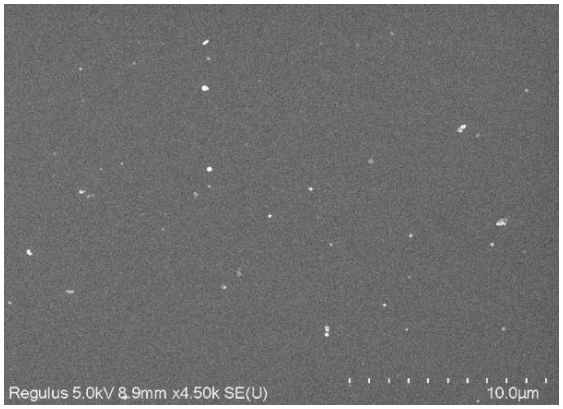

Figure 17 - Scanning electron microscope (SEM) image of the SnO_2 (10%) thin film.

3.2.3 Perovskite characterization

3.2.3.1 Optical characterization

The UV-visible absorbance spectra for $MAPbI_3$ films deposited on SnO_2 (10%) and E-SnO_2 (10%) ETLs is shown in Figure 18 (a). Figure 18 (b) shows the corresponding Tauc Plots for the absorption spectra. The absorbance spectra show that $MAPbI_3$ film deposited on E-SnO_2 has a higher absorbance than SnO_2 in the visible wavelength range from 400 to 800 nm. The bandgap value obtained for the perovskite films on SnO_2 and E-SnO_2 ETLs was 1.59 eV for both films. Figure 18 (c) shows the steady-state PL spectra for the perovskite films deposited on SnO_2 and E-SnO_2 ETLs. The perovskite film on E-SnO_2 showed a weaker PL suggesting that the carriers are extracted more efficiently.

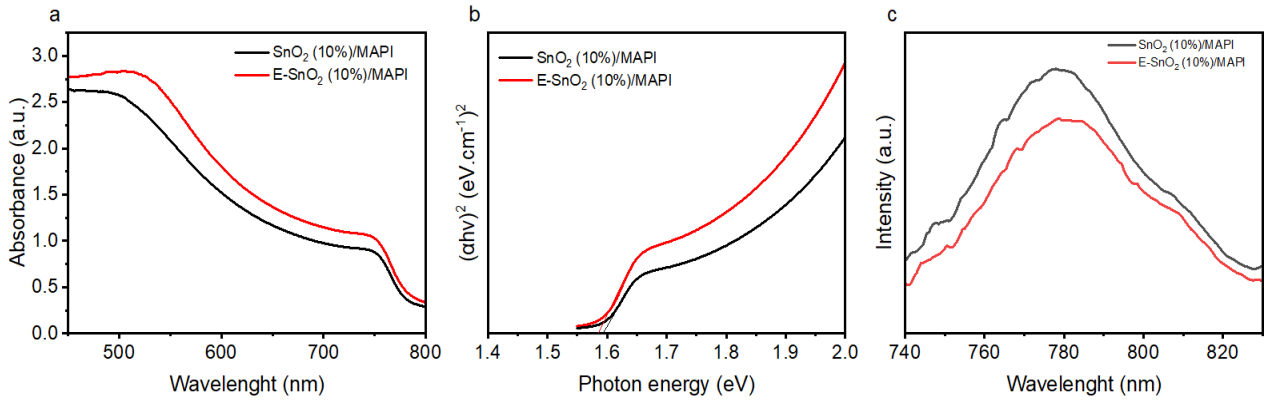

Figure 18 - a) UV–Vis absorption spectra, b) Tauc plot and c) PL spectra of the $MAPbI_3$ films deposited on SnO_2 (10%) and E-SnO_2 (10%).

3.2.3.2 Structural characterization

Figure 19 (a) and (b) show the XRD pattern of the $MAPbI_3$ films deposited on SnO_2 and E-SnO_2, respectively. The dominant diffraction peaks correspond to the $MAPbI_3$ tetragonal structure. In the E-SnO_2 graph, there is one extra peak located at the angle 2θ of 12.5° which is assigned to the (001) peak of PbI_2. It has been reported that PbI_2 on the perovskite film's surface might heal the halide vacancy generating type-I band alignment and reduce the trap state density [48].

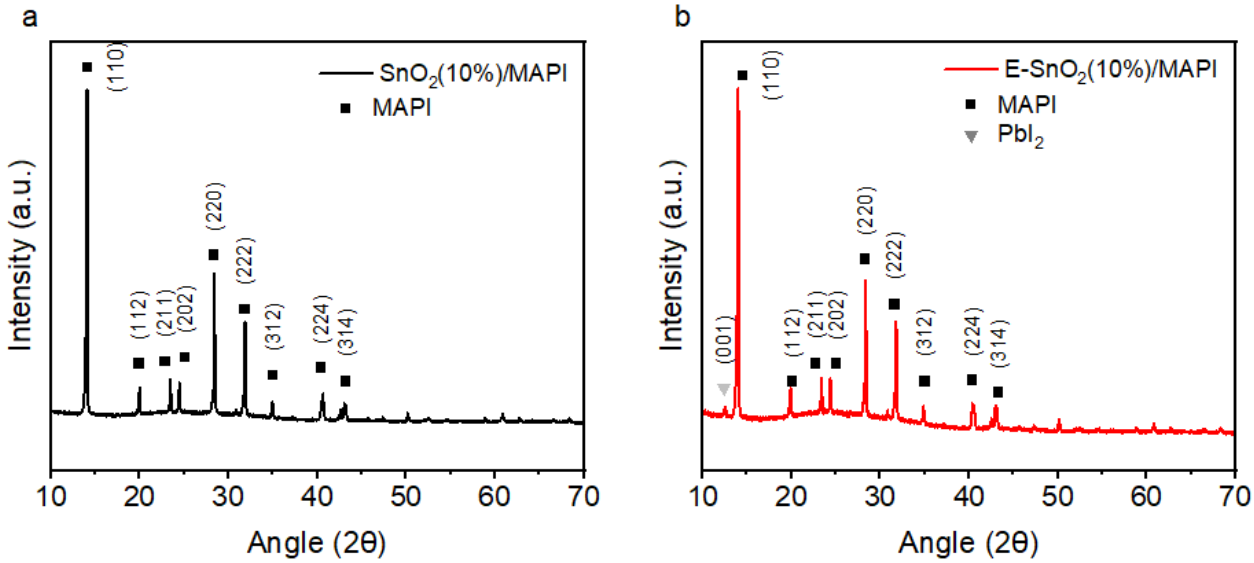

Figure 19 - X-ray diffraction (XRD) spectra of a $MAPbI_3$ film prepared on a) SnO_2 (10%) and b) E-SnO_2 (10%).

The surface morphology of the perovskite films was also analyzed by SEM analysis. Figure 20 (a) and (b) show the top-view SEM images of the perovskite films deposited on SnO_2 (10%) and E-SnO_2 (10%) ETLs, respectively. Perovskite film on SnO_2 shows a film with small grains, having various shapes, sizes, and large number of pinholes. Figure 20 (b) shows the perovskite film deposited on E-SnO_2 having bigger grains size with various shapes and sizes. It has smaller number of pinholes in-between the grains than that for SnO_2. The box plot for the grain size distribution of the perovskite films deposited on both ETLs is represented Figure 20 (c). It demonstrates that the perovskite deposited on E-SnO_2 has a larger average grain size which is around 1.1 µm, while, SnO_2 has an average grain size of 0.52 µm which is co-related with the device efficiency as the GBs are the major recombination centers [49].

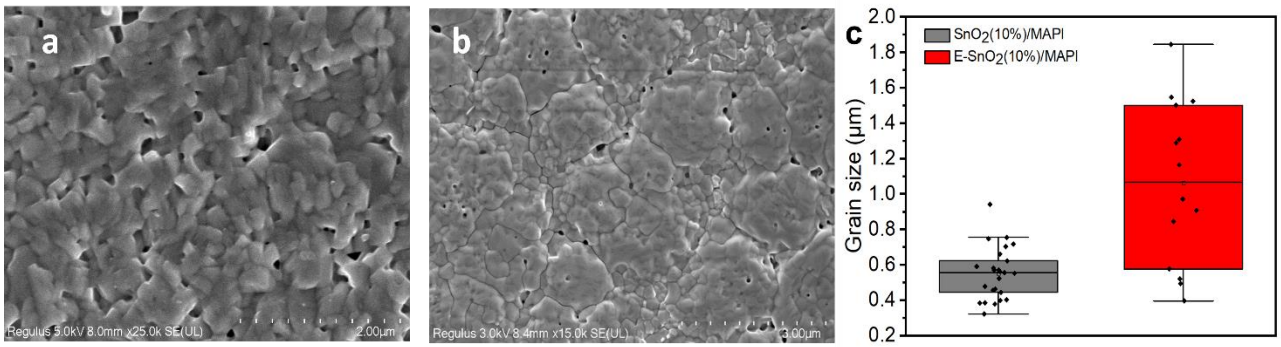

Figure 20 - Top-view SEM images of $MAPbI_3$ on a) SnO_2 (10%) and b) E-SnO_2 (10%). c) Grain size distribution of the $MAPbI_3$ films.

3.3 For SnO_2 and E-SnO_2 (7.5%) based ETL

3.3.1 Electrical Characterization of the solar cells

PSCs with 7.5% concentration of SnO_2 and E-SnO_2 based ETLs were developed and their optical, structural, and electrical properties were studied in the same way as the previous concentrations. Figure 21 (a-d) shows the box chart of the best performing solar cells parameters. The devices based on E-SnO_2 ETL have a higher V_{OC} because of the improved band allignment with perovskite. The efficiency for the E-SnO_2 based solar cells are higher than the only SnO_2 based cells due to higher V_{OC} and FF. The parameters for the best cell are described below.

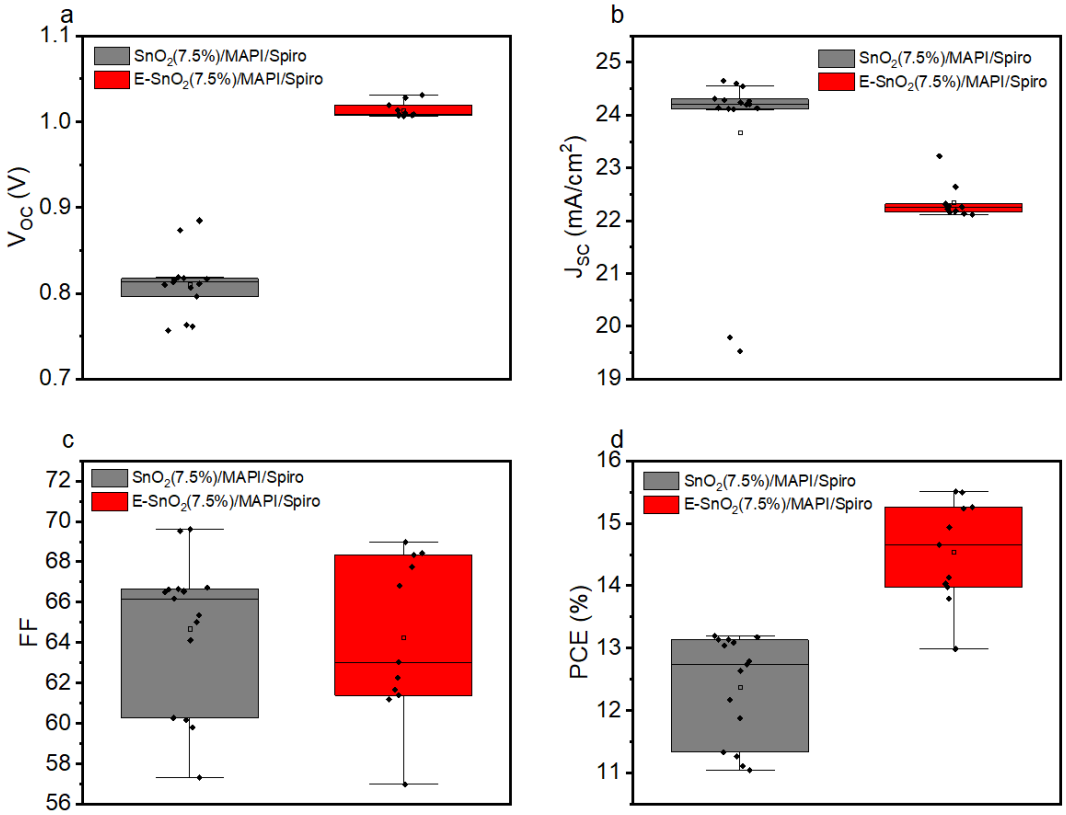

Figure 21 – (a) V_{OC}, (b) J_{SC}, (c) FF and (d) PCE distributions of PSCs with SnO_2 (7.5%) and E-SnO_2 (7.5%) based ETLs.

3.3.2 *J-V* curve for the best solar cell

Figure 22 (a) shows the *J-V* curve of the best performing cell for 7.5% SnO_2 and E- SnO_2 based ETL. The best device for SnO_2 based ETL shows a PCE of 13.20% where Jsc=24.31 mA/cm^2, Voc=0.82 V and FF=66.50. The E-SnO_2 ETL based device shows PCE of 15.51% with the value of J_{SC}=22.18 mA/cm^2, V_{oc}=1.01 V and FF=68.97. Figure 22 (b) shows the corresponding EQE spectra for both cells. From the EQE spectra the J_{SC} values were calculated which are 21.38 mA/cm^2 for the SnO_2 and 20.36 mA/cm^2 for the E-SnO_2 based solar cells.

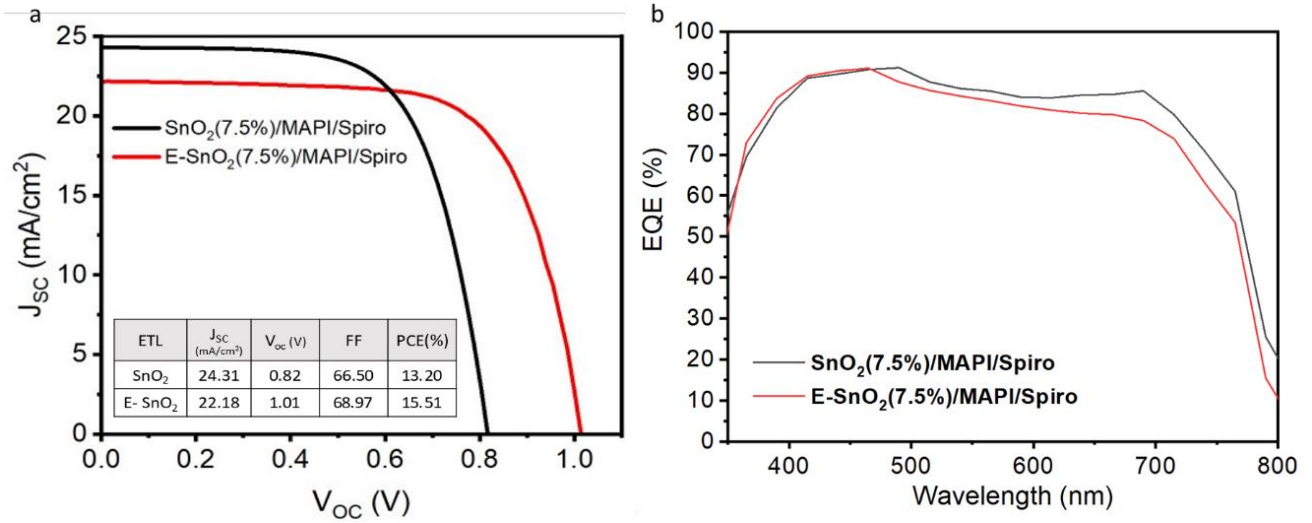

Figure 22 – a) *J-V* curves of the best performing devices based on SnO_2 (7.5%) and E-SnO_2 (7.5%). b) EQE spectra for those PSCs.

In order to evaluate the long-term stability performance for both SnO_2 and E-SnO_2 based best cells, these were stored in vacuum. Their PCE were measured over time as shown in Figure 23. After 700h, the SnO_2 device performance decreased to 62% of its initial PCE while the E-SnO_2 based PSC only decreased to 83%. This shows that by complexing EDTA with SnO_2, the long-term stability of the device can be improved.

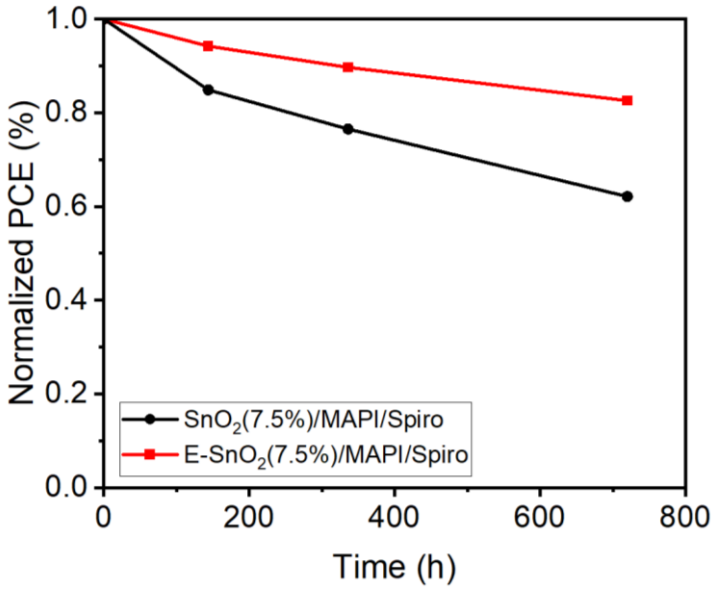

Figure 23 - Long-term stability performance of the best performing PSCs based on SnO_2 (7.5%) and E-SnO_2 (7.5%) ETLs.

3.3.3 ETL characterization

3.3.3.1 Optical characterization

UV-Vis spectrophotometry was used to analyze the optical properties of the different ETL layers. Figure 24 (a) shows the optical transmission spectra for SnO_2 (7.5%) and E-SnO_2 (7.5%) deposited on ITO. E-SnO_2 demonstrates a higher transmission for wavelengths higher than 500 nm and both samples show good optical properties with transmission values over 85% across visible region. Figure 24 (b) shows the bandgaps of each ETL which were extrapolated from the Tauc plots the calculated bandgaps for the SnO_2 and E-SnO_2 were 4.15 and 4.16 eV, respectively.

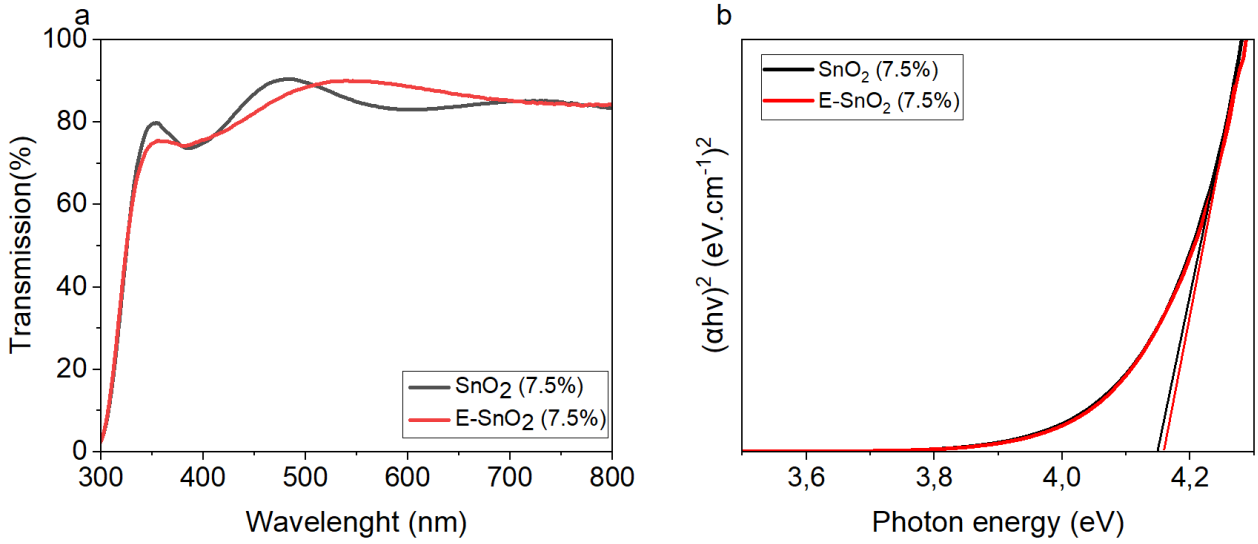

Figure 24 – a) Transmission plot for SnO_2 (7.5%) and E-SnO_2 (7.5%) samples. b) Tauc plot (with slope) of the same samples.

3.3.3.2 Structural characterization

To obtain insights about the SnO_2 and E-SnO_2 films, structural characterization was performed. Figure 25 shows the XRD pattern for the (a) SnO_2 and (b) E-SnO_2 films, respectively. By analyzing Figure 25 (a), like the other concentrations, the peaks for SnO2 are not very intense which indicates that there was only a partial crystallization of the SnO_2. For E-SnO_2, the peaks are less visible due to poor crystallization.

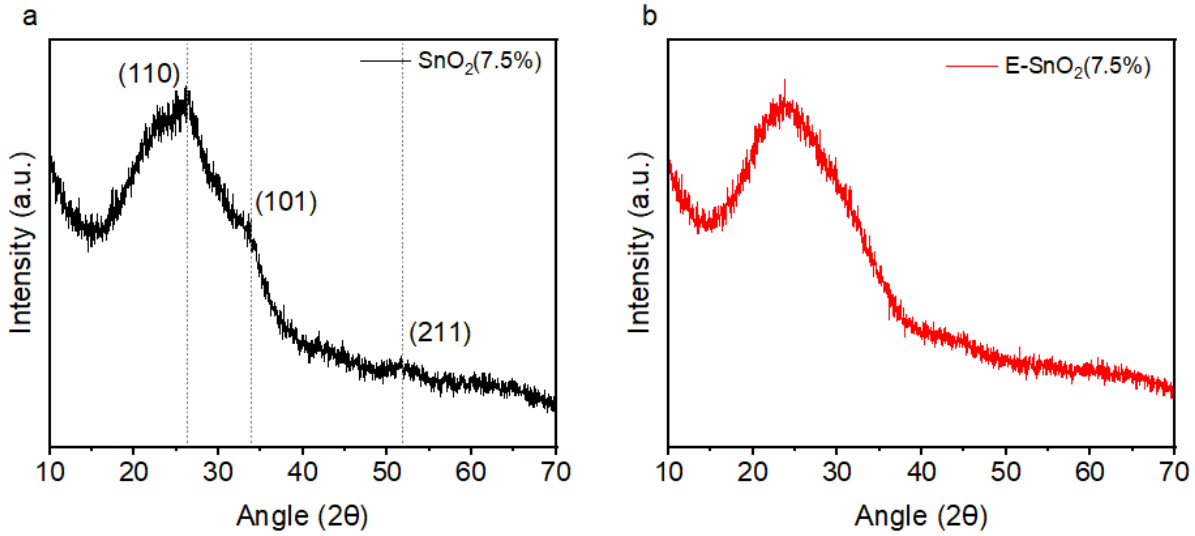

Figure 25 - X-ray diffraction pattern of the a) SnO_2 (7.5%) and b) E-SnO_2 (7.5%) thin film.

The top-view SEM image for the SnO_2 film is shown in Figure 26. It shows a flat, uniform, and smooth film with no defects.

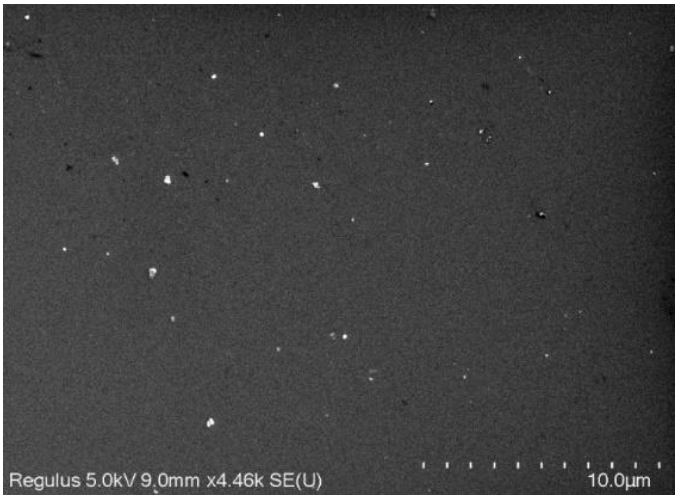

Figure 26 - Scanning electron microscope (SEM) image of SnO_2 (7.5%) thin film

After comparing the results for different concentrations, it is concluded that 7.5 % is the best percentage for E-SnO_2 based PSCs. Therefore, different other extra characterizations for ETLs and perovskite layers were also performed for this concentration.

An atomic force microscopy (AFM) analysis was performed on the SnO_2 and E-SnO_2 films to study the morphological properties of the films. Figure 27 (a) and (b) show the AFM topography images of the SnO_2 and E-SnO_2 films, respectively. Gwydion software was used to measure the root mean square (RMS) roughness of the films. The images reveal that the root-mean-square (RMS) roughness for SnO_2, E-SnO_2 films are 29.38 nm and 7.38 nm, respectively. It is clear that after the EDTA treatment, the roughness exceptionally decreases for the combined E-SnO_2 film which is an important parameter for better development of perovskite layer for high performance PSCs. In addition, the electron mobility for these films is shown in Table 2 measured by the Hall effect measurement system. This shows that the electron mobility of the combined E-SnO_2 film is 140 $cm^2V^{-1}S^{-1}$ which is much higher than that for only SnO_2 which is 36.8 $cm^2V^{-1}S^{-1}$. It is obvious that the large electron mobility of the ETL benefits to extract charge carriers from the absorber layer avoiding recombination.

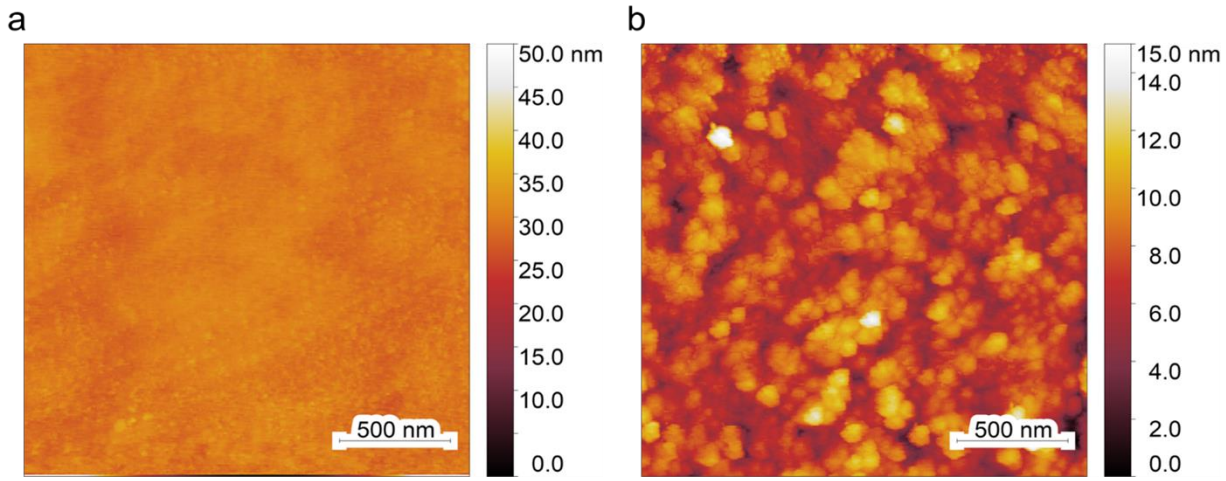

Figure 27 - AFM topographical images of a) SnO_2 (7.5%) and b) E-SnO_2 (7.5%) films.

Table 2 - Data of Hall mobility, carrier concentration and sheet resistance for SnO_2 and E-SnO_2 films.

Samples	Hall mobility ($cm^2V^{-1}s^{-1}$)	Carrier concentration (cm^{-3})	Sheet resistance (Ohm/sq))
SnO_2	36.8	9.09×10^{11}	6.21×10^{9}
E-SnO_2	140	9.45×10^{12}	1.58×10^{9}

3.3.4 Perovskite characterization

3.3.4.1 Optical characterization

The UV-visible absorbance spectra for $MAPbI_3$ films deposited on SnO_2 (7.5%) and E-SnO_2 (7.5%) ETLs are shown in Figure 28 (a). Figure 28 (b) shows the corresponding Tauc Plots for these absorbance spectra. The absorbance spectra show that $MAPbI_3$ film deposited on E-SnO_2 has the same absorbance as SnO_2 in the visible wavelength range from 400 to 800 nm. The band gap of the perovskites has been calculated in the same way as the other concentrations which is described in chapter 3.1.4.1. The bandgap value obtained for the perovskite films on SnO_2 and E-SnO_2 ETLs was 1.59 eV for both films. The recombination kinetics of the perovskite films deposited on SnO_2 and E-SnO_2 ETLs has been observed by steady-state PL analysis shown in Figure 28 (c). The perovskite film on E-SnO_2 showed a much weaker PL suggesting that the carriers are extracted more efficiently.

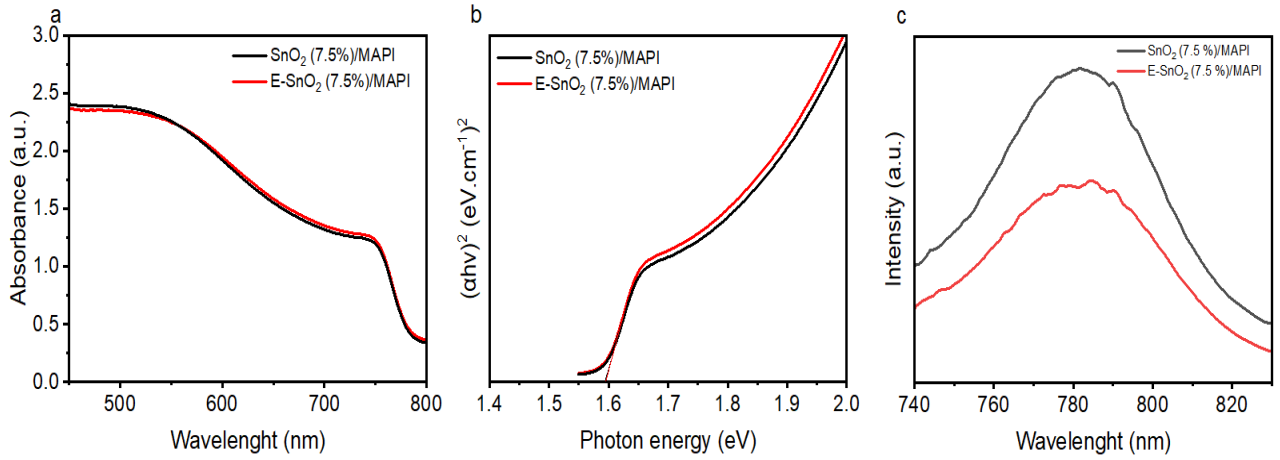

Figure 28 - a) UV–Vis absorption spectra, b) Tauc plot and c) PL spectra of the $MAPbI_3$ films deposited on SnO_2 (7.5%) and E-SnO_2 (7.5%).

3.3.4.2 Structural characterization

To know about the crystalline structure of the perovskite films, X-ray diffraction analysis (XRD) was performed. Figure 29 (a) and (b) show the characteristic peaks of the $MAPbI_3$ film deposited on SnO_2 and E-SnO_2. The dominant diffraction peaks correspond to the $MAPbI_3$ tetragonal structure. In both graphs, there is one peak located at the angle 2θ of 12.5° which is assigned to the (001) peak of PbI_2. Figure 48 (appendix) demonstrates that this peak is more intense for the E-SnO_2 based perovskite film with 7.5% concentration than the other concentrations. Figure 47 (appendix) also shows the top-view SEM images of the $MAPbI_3$ on E-SnO_2 film containing PbI_2 grains.

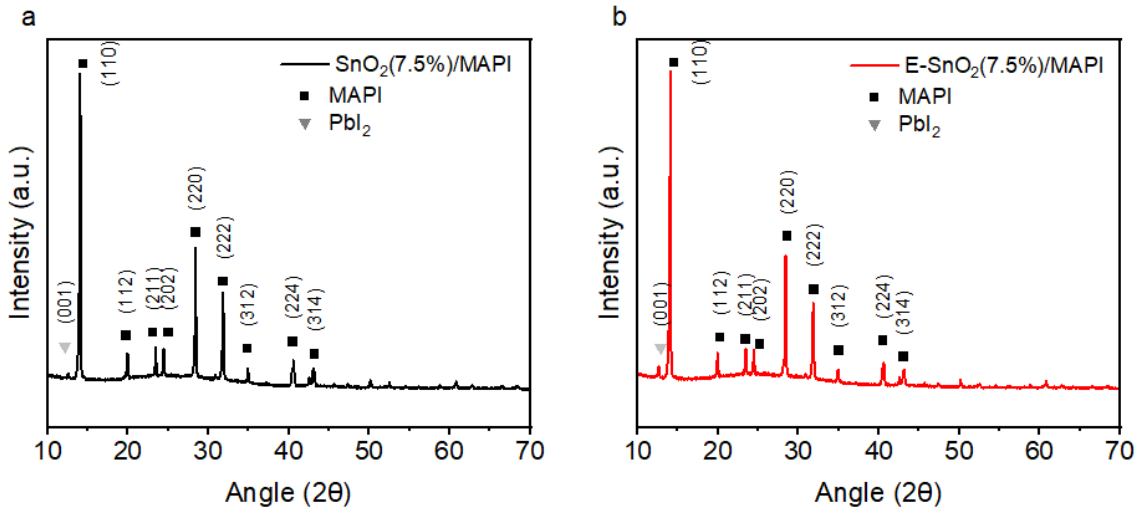

Figure 29 - X-ray diffraction (XRD) spectra of a $MAPbI_3$ film prepared on a) SnO_2 (7.5%) and b) E-SnO_2 (7.5%).

The surface morphology of the perovskite films was analyzed by using SEM. Figure 30 (a) and (b) show the top-view SEM images of the perovskite films deposited on SnO_2 (7.5%) and E-SnO_2 (7.5%) ETLs, respectively. Perovskite film on SnO_2 (Figure 30 a) shows big grains, with various shapes and sizes but some pinholes. Figure 30 (b) shows the perovskite film deposited on E-SnO_2 with bigger grains and a greatly reduced number of pinholes than that for SnO_2. The box plot for the grain size distribution of the perovskite films deposited on both ETLs is represented in Figure 30 (c) and its demonstrates that the perovskite deposited on E-SnO_2 has a larger average grain size which is around 1.21 µm while SnO_2 has an average grain size of 1.03 µm.

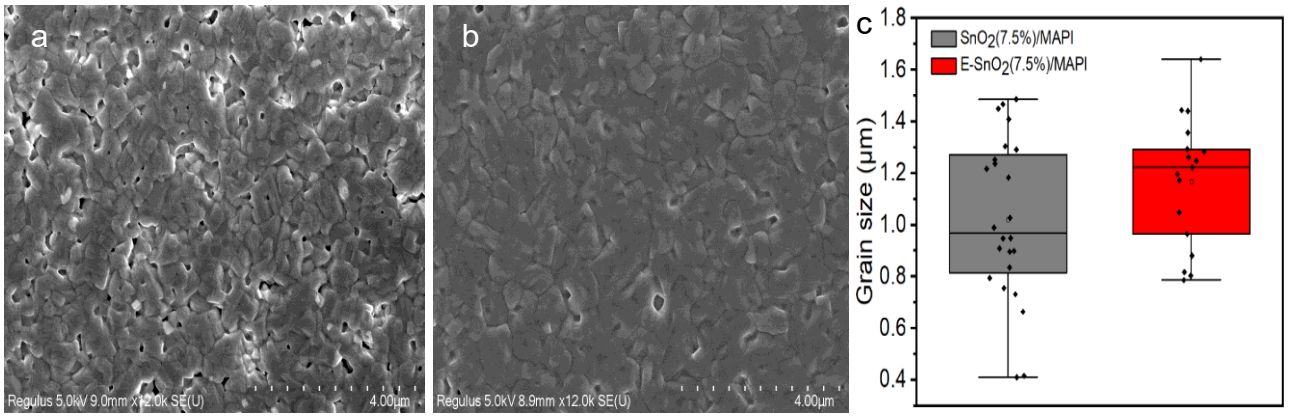

Figure 30 - Top-view SEM images of $MAPbI_3$ on a) SnO_2 (7.5%) and b) E-SnO_2 (7.5%). c) Grain size distribution of the $MAPbI_3$ films.

Figure 31 (a) shows the full XPS spectra for the perovskite films deposited on SnO_2 (7.5 %) and E-SnO_2 (7.5 %) ETLs, respectively. These spectra show the four main peaks centered at 138 eV, 286 eV, 402 eV and 619 eV, which were assigned to Pb 4f, C 1s, N 1s and I 3d, respectively. The high resolution XPS spectra for Pb 4f and I 3d peaks are shown in Figure 31 (b) and (c), respectively. For only SnO_2 based MAPI film, the peaks of Pb $4f_{5/2}$ and Pb $4f_{7/2}$ were detected at 143.5 eV and 138.5 eV, respectively. For E-SnO_2 based ETL, the Pb 4f peak pairs shifted to a slightly lower binding energy. A decrease in binding energy results from an increase in the electron screening effect as a result of an increase in electron density [50]. This redshift in the binding energy can therefore be tentatively attributed to the interactions between uncoordinated PbI_2 and the electron-rich N and O atoms, which increase the electron cloud density and decrease the electron affinity of PbI_2 ions [51].

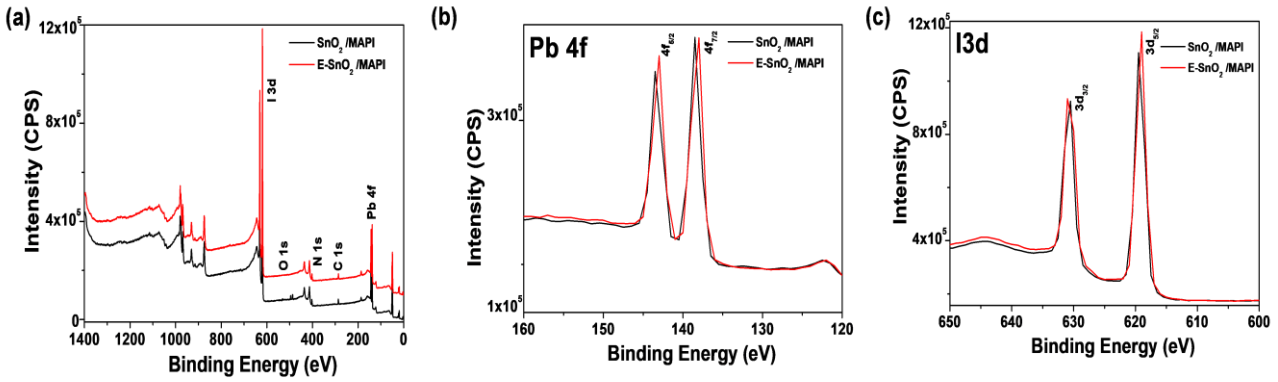

Figure 31 - a) XPS spectra of MAPbI3 film deposited on SnO2 (7.5%) and E-SnO2 (7.5%). b) Pb 4f XPS spectra of $MAPbI_3$. c) I 3d XPS spectra of $MAPbI_3$.

Kelvin probe force microscopy (KPFM) was also used to measure the surface potential of the perovskite layers. The contact potential difference (CPD) between the microscope metal tip and the perovskite surface gives the values of their surface potential. Figure 32 shows the CPD map of $MAPbI_3$ films deposited on both ETLs. It is clear to see that the sample where $MAPbI_3$ is deposited on E-SnO_2 has a higher surface potential which is around 370 mV while the perovskite on SnO_2 is around 230 mV. These findings show that E-SnO_2 based perovskite results in a higher Fermi energy level, which provides a superior band alignment between the ETL and the perovskite [52].

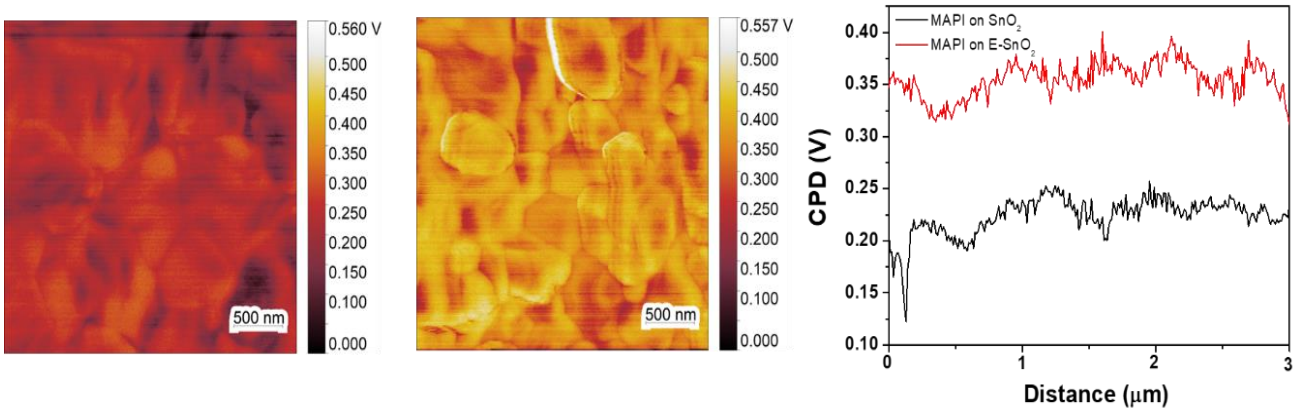

Figure 32 - CPD distribution of the $MAPbI_3$ perovskite film on a) SnO_2 and b) E-SnO_2. c) Line profile of surface potential of the films.

3.4 For SnO_2 and E-SnO_2 (2.5%) based ETL

3.4.1 Electrical Characterization of the solar cells

PSCs with 2.5% concentration of SnO_2 and E-SnO_2 based ETLs were fabricated the same way as the other concentrations. Figure 33 shows the box chart of the best performing solar cells parameters. The devices based on E-SnO_2 ETL have average higher V_{OC} and Jsc values than the SnO_2 ones. The parameters for the best cell are described below.

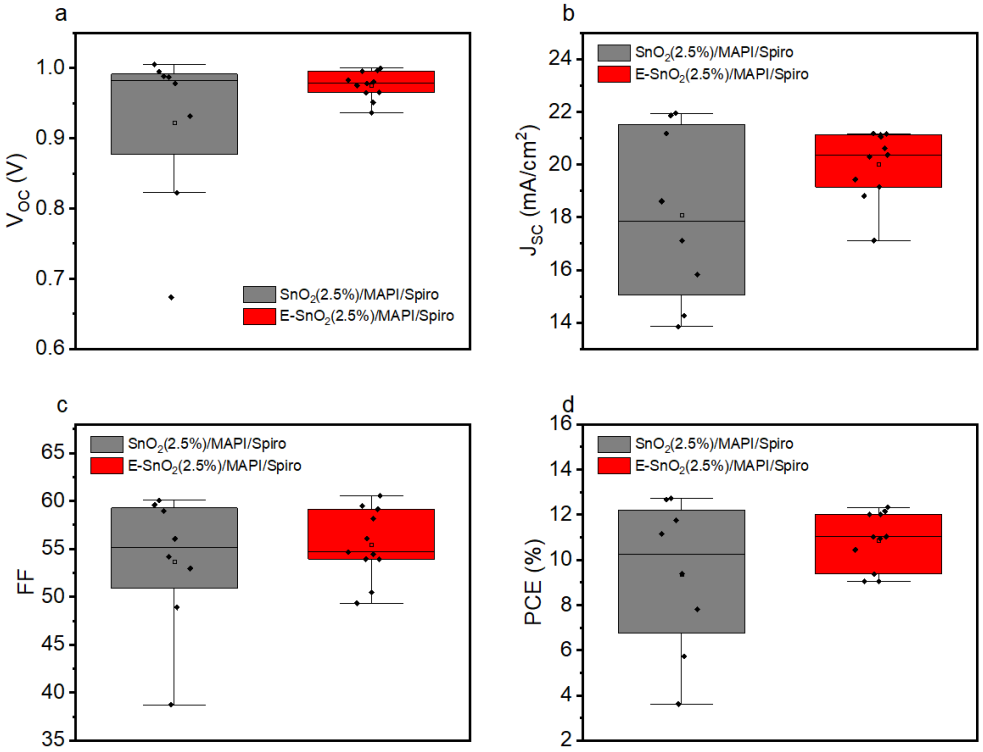

Figure 33 - (a) V_{OC}, (b) J_{SC}, (c) FF and (d) PCE distributions of PSCs with SnO_2 (2.5%) and E-SnO_2 (2.5%) based ETLs.

3.4.2 *J-V* curve for the best solar cell

The *J-V* curve for the best performing cell for 2.5% SnO_2 and E-SnO_2 based ETLs is illustrated in Figure 34 (a). The best cell for SnO_2 based ETL has a PCE of 12.66% where Jsc=21.19 mA/cm^2, Voc=0.99 V and FF=60.08. On the other hand, the E-SnO_2 ETL based device shows a PCE of 12.33% with the value of J_{SC}=20.37 mA/cm^2, V_{oc}=1.00 V and FF=60.54. Figure 34 (b) shows the EQE spectra for the corresponding best cells. From the EQE spectra, the J_{SC} values were calculated, and these are 20.30 mA/cm^2 for the device with SnO_2 ETL and 19.36 mA/cm^2 for the device with E-SnO_2 ETL.

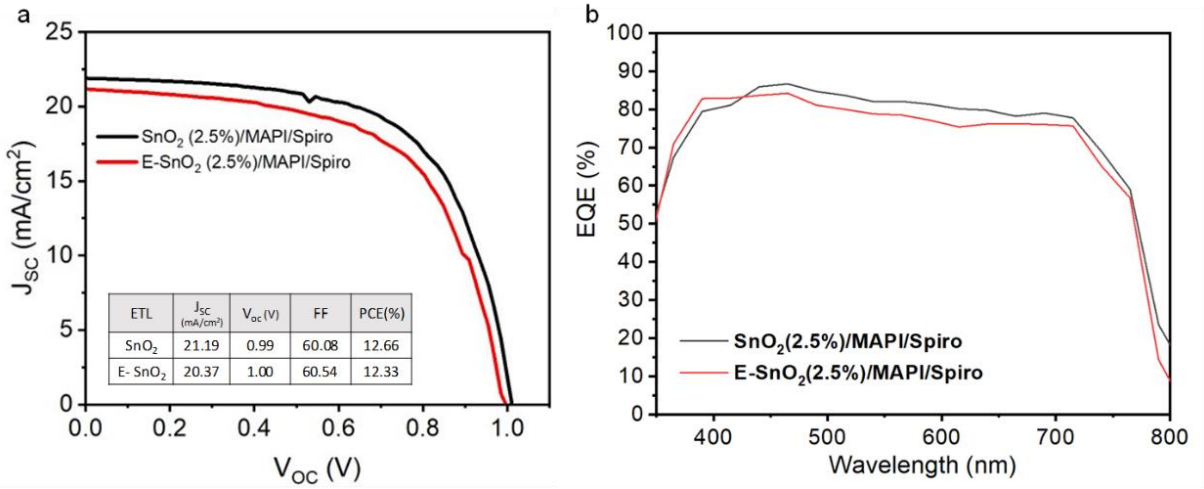

Figure 34 – a) *J-V* curves of the best performing PSCs based on SnO_2 (2.5%) and E-SnO_2 (2.5%) ETLs b) EQE spectra of the PSCs.

3.4.3 ETL characterization

3.4.3.1 Optical characterization

Figure 35 (a) shows the optical transmission spectra for SnO_2 (2.5 %) and E-SnO_2 (2.5 %) films deposited on ITO. Both SnO_2 and E-SnO_2 samples demonstrate a similar optical transmission spectrum across the visible region with values over 80 %. The calculated bandgap (from Figure 35 b) for the SnO_2 and E-SnO_2 was 4.12 eV for both samples.

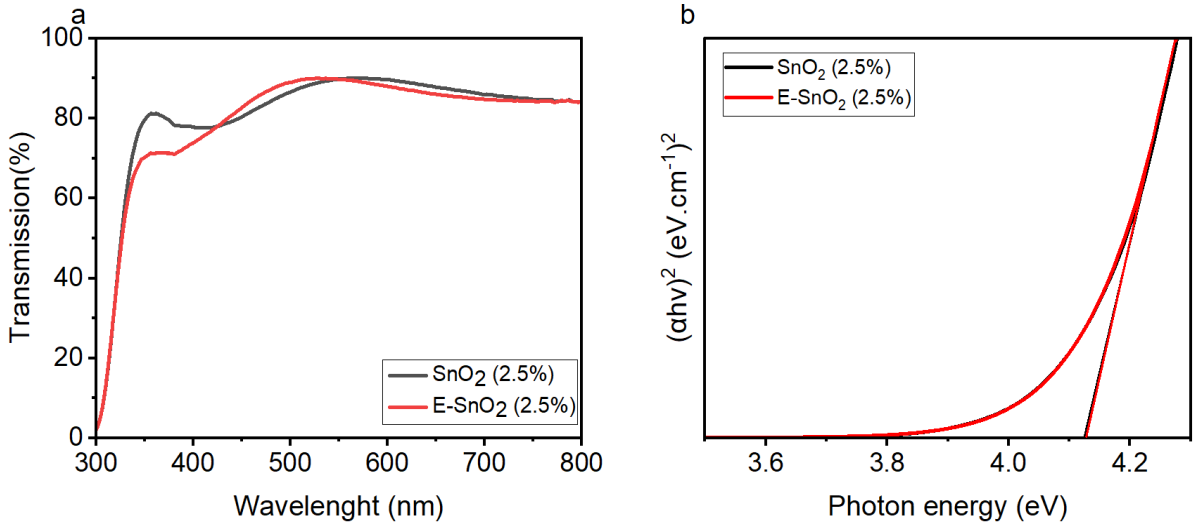

Figure 35 – a) Transmission plot of SnO_2 (2.5%) and E-SnO_2 (2.5%) samples. b) Tauc plot (with slope) of the same samples.

3.4.3.2 Structural characterization

To obtain insights about the SnO_2 and E-SnO_2 films, structural characterization using X-ray diffraction (XRD) analysis was performed. Figure 36 shows the XRD pattern for the (a) SnO_2 and (b) E-SnO_2 films, respectively. As the percentage of SnO_2 solution is low, therefore, for this concentration, the X-ray diffractograms for both films don't show any peaks associated with SnO_2 which indicates that both films possess very poor crystallinity.

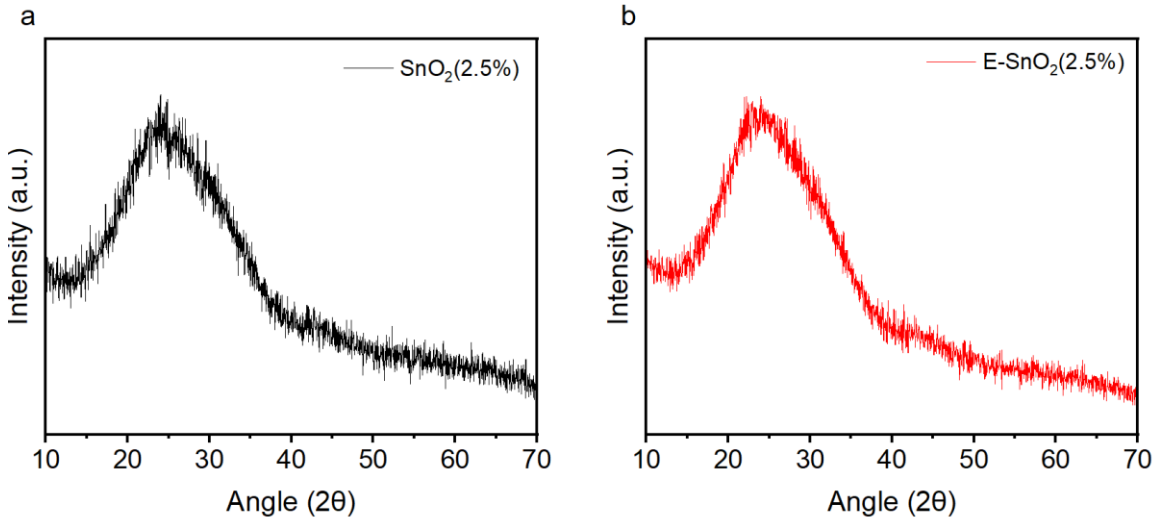

Figure 36 - X-ray diffraction pattern of the a) SnO_2 (2.5%) and b) E-SnO_2 (2.5%) thin film.

The top-view SEM characterization was performed in order to obtain information about the morphology of the SnO_2 films deposited on ITO. Figure 37 shows the top-view SEM image of a film with some defects present and with some roughness associated.

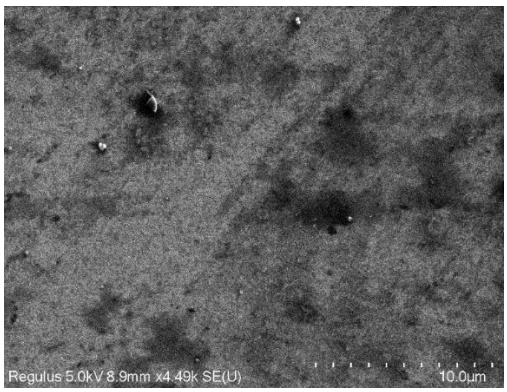

Figure 37 - Scanning electron microscope (SEM) image of SnO_2 (2.5%) thin film

3.4.4 Perovskite characterization

3.4.4.1 Optical characterization

The UV-visible absorbance spectra for $MAPbI_3$ films deposited on SnO_2 (2.5%) and E-SnO_2 (2.5%) ETLs are shown in Figure 38 (a). Figure 38 (b) shows the corresponding Tauc Plots for these absorbance spectra. The $MAPbI_3$ film deposited on E-SnO_2 has the same absorbance as the $MAPbI_3$ film deposited on SnO_2 in the wavelength range between 600 and 800 nm, whereas the SnO_2 one has higher absorbance for wavelength values below 600 nm. The bandgap value obtained for the perovskite films on SnO_2 and E-SnO_2 ETLs was 1.6 eV for both films. The recombination kinetics of the perovskite films deposited on SnO_2 and E-SnO_2 ETLs has been observed by steady-state PL analysis shown in Figure 38 (c). The perovskite film on E-SnO_2 showed a weaker PL demonstrating that carriers are extracted more efficiently.

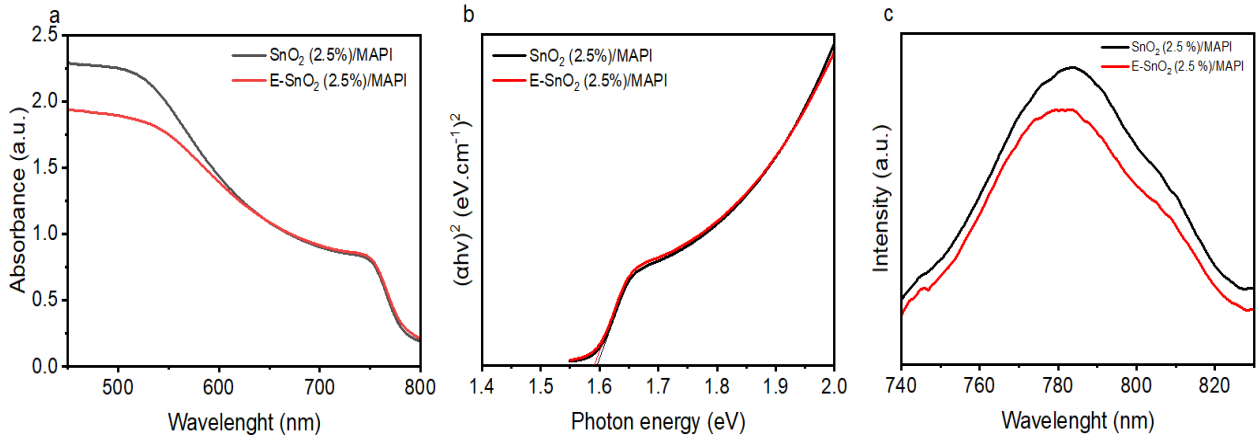

Figure 38 - a) UV–Vis absorption spectra, b) Tauc plot and c) PL spectra of the $MAPbI_3$ films deposited on SnO_2 (2.5%) and E-SnO_2 (2.5%).

3.4.4.2 Structural characterization

To know about the crystalline structure of the perovskite films, X-ray diffraction analysis (XRD) was performed. Figure 39 (a) and (b) show the characteristic peaks of the $MAPbI_3$ film deposited on SnO_2 and E-SnO_2 ETLs, respectively. The dominant diffraction peaks correspond to the lattice planes of the $MAPbI_3$ tetragonal structure. In both graphs, there is one peak located at the angle 2θ of 12.5° which is assigned to the (001) peak of PbI_2. In comparison with the other concentrations, both diffractograms have the lowest intensity peaks as shown in Figure 46 (appendix).

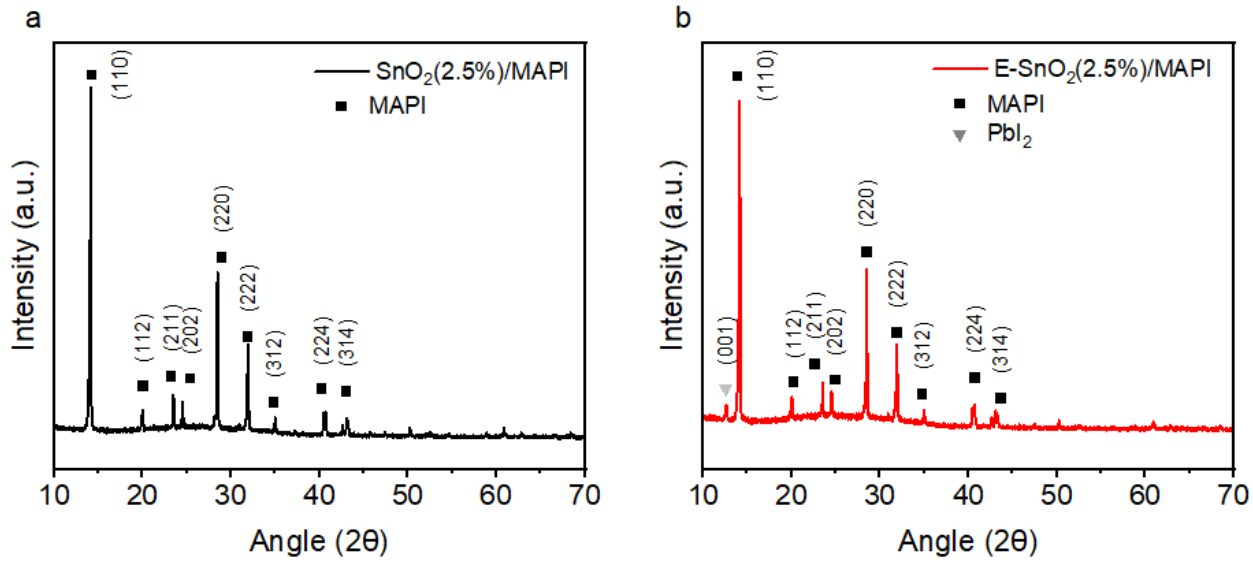

Figure 39 - X-ray diffraction (XRD) spectra of a $MAPbI_3$ film prepared on a) SnO_2 (2.5%) and b) E-SnO_2 (2.5%).

The surface morphology of the perovskite films was analyzed by using SEM. Figure 40 (a) and (b) show the top-view SEM images of the perovskite films deposited on SnO_2 (2.5%) and E-SnO_2 (2.5%) ETLs, respectively. Perovskite film on SnO_2 shows a film with small grains and with some pinholes. Figure 40 (b) shows the perovskite film deposited on E-SnO_2 with the same average grain size and with roughly the same number of pinholes as SnO_2. The box plot for the grain size distribution of the perovskite films deposited on both ETLs is represented in Figure 40 (c) and its demonstrates that the perovskite deposited on E-SnO_2 has a grain size around 0.45 µm while SnO_2 has an average grain size of 0.40 µm.

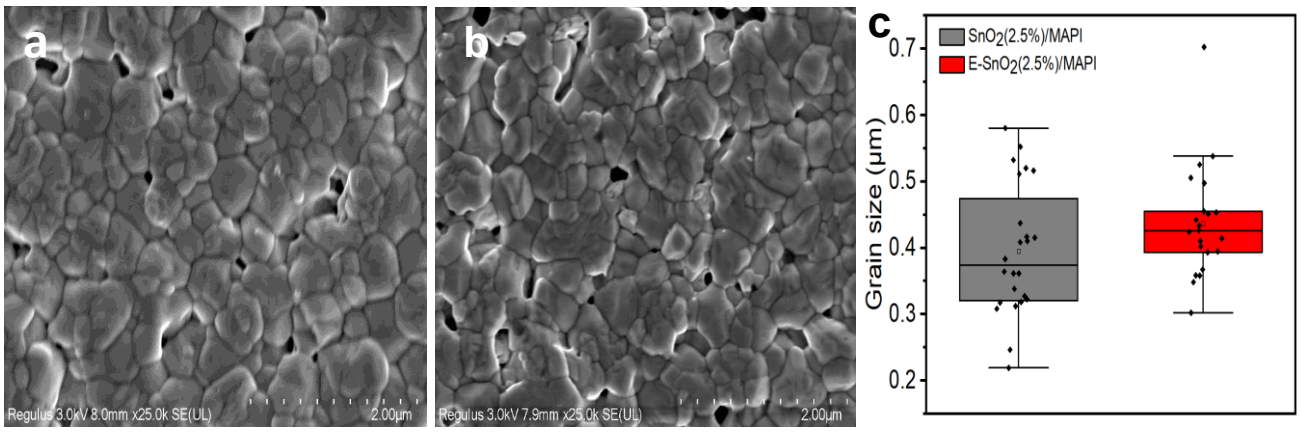

Figure 40 - Top-view SEM images of $MAPbI_3$ on a) SnO_2 (2.5%) and b) E-SnO_2 (2.5%). c) Grain size distribution of the $MAPbI_3$ films.

4

CONCLUSIONS AND FUTURE PERSPECTIVES

In summary, an effective way has been demonstrated to improve the performances of the planar PSCs by modifying the SnO_2 ETL with EDTA. During the project, large number of photovoltaic devices were developed by using four different concentrations of SnO_2 and E-SnO_2 based ETLs. All solutions were prepared and deposited outside of the glove box.

The basic structure of the solar cell is ITO/SnO_2 (E-SnO_2)/MAPI/HTL/Au. Four different percentages of SnO_2 and E-SnO_2 solutions were utilized to make ETL for each PSC structure, and they were characterized by optically, structurally, morphologically, and electrically. Mixing of EDTA with SnO_2 improved not only the electrical conductivity of SnO_2, but also the crystallization and surface potential of the perovskite layer that was placed on top, resulting in improved photovoltaic performance. A comparison study between the ETLs (SnO_2 and E-SnO_2) was also performed for all concentrations. Both ETLs showed high optical transmittance in the visible region and a large optical bandgap. From the XRD analysis, it was concluded that the SnO_2 films were partially crystalline, while, the E-SnO_2 films were less crystalline due to low annealing temperature processing technique. It was also observed from the AFM analysis that the E-SnO_2 film possessed a lower surface roughness than the bare SnO_2 film which is advantageous for perovskite film deposition on top of that. When perovskite film is deposited on E-SnO_2 ETLs, it has better benefits, such as larger grains, less trap density, and high crystallinity. These benefits are linked to the high performance of planar-type PSCs. The presence of PbI_2 peak is clearly observed in XRD analysis for all concentrations E-SnO_2 based perovskite films. But the peak intensity is highest for 7.5% E-SnO_2 based perovskite films. In this case, the SEM image also reveals that PbI_2 is present on the GBs and surfaces of the perovskite film. For all percentage, the perovskite film on E-SnO_2 revealed significantly weaker PL intensity demonstrating that carriers are extracted more efficiently. The presence of PbI_2 in perovskite helps to reduce the point defects, resulting the nonradiative recombination is suppressed. In the meantime, the KPFM results for 7.5 % SnO_2 and E-SnO_2 based perovskite films also suggest that the presence of PbI_2 causes an upward shift of the Fermi level towards the conduction band. This shift has the potential to enhance the difference between the Fermi level of electrons (E_{Fn}) and the Fermi level of holes (E_{Fp}) when exposed to light. Consequently, the open circuit voltage (V_{OC}) experienced a rise from 0.82 V to 1.01 V causes of the efficiency enhancement from 13.20% to 15.51%. These results showed that E-SnO_2 is an excellent ETL in PSCs. In the future, more work needs to be done to precisely control E-SnO_2 ETL, including film quality, defects, and surface states. This will make it more effective at charge transfer by lowering interface recombination and energy loss.

4.1 Future Perspectives

To further enhance this work, it would be advantageous to conduct additional studies and measurements. Performing an Ultraviolet Photoelectron spectroscopy (UPS) would be a good starting point since it allows to get better insights about the band structure and work function of the ETLs. A Time-Resolved Photoluminescence

(TRPL) analysis would also be beneficial to complement this work since it allows for a better understanding of the recombination kinetics of the perovskite films [53].

It would also be interesting to explore some other parameters of the ETL deposition, the annealing time and temperature since it influences the morphology of the films. Changing the deposition type of the SnO_2 from spin coating to ultrasonic spraying would also be a good approach because it produces a SnO_2 films with wider bandgap, lower surface roughness and higher carrier concentration. The PSCs produced with sprayed SnO_2 would also have a higher efficiency and are more suitable for large area depositions [44].

Some extra investigation about the perovskite layer should also be performed such as changing the reagents concentration of the perovskite or even change the perovskite and see how it affects the parameters of the solar cells.

BIBLIOGRAPHY

[1] M. K. H. Rabaia *et al.*, "Environmental impacts of solar energy systems: A review," *Science of the Total Environment*, vol. 754, Feb. 2021, doi: 10.1016/j.scitotenv.2020.141989.

[2] Y. Chen, M. Zhang, F. Li, and Z. Yang, "Recent Progress in Perovskite Solar Cells: Status and Future," *Coatings*, vol. 13, no. 3. MDPI, Mar. 01, 2023. doi: 10.3390/coatings13030644.

[3] "PEROVSKITE SOLAR CELLS_A BRIEF INTRODUCTION AND".

[4] S. Yun *et al.*, "New-generation integrated devices based on dye-sensitized and perovskite solar cells," *Energy and Environmental Science*, vol. 11, no. 3. Royal Society of Chemistry, pp. 476–526, Mar. 01, 2018. doi: 10.1039/c7ee03165c.

[5] N. Shah *et al.*, "A Review of Third Generation Solar Cells," *Processes*, vol. 11, no. 6, p. 1852, Jun. 2023, doi: 10.3390/pr11061852.

[6] J. Duan *et al.*, "Inorganic perovskite solar cells: an emerging member of the photovoltaic community," *J Mater Chem A Mater*, vol. 7, no. 37, pp. 21036–21068, 2019, doi: 10.1039/C9TA06674H.

[7] Y. Rong *et al.*, "Challenges for commercializing perovskite solar cells," *Science*, vol. 361, no. 6408. American Association for the Advancement of Science, Sep. 21, 2018. doi: 10.1126/science.aat8235.

[8] "cell-pv-eff-emergingpv".

[9] J. P. Attfield, P. Lightfoot, and R. E. Morris, "Perovskites," *Dalton Transactions*, vol. 44, no. 23, pp. 10541–10542, 2015, doi: 10.1039/C5DT90083B.

[10] E. A. Katz, "Perovskite: Name Puzzle and German-Russian Odyssey of Discovery," *Helvetica Chimica Acta*, vol. 103, no. 6. Wiley Blackwell, Jun. 01, 2020. doi: 10.1002/hlca.202000061.

[11] Z. Xiao, Z. Song, and Y. Yan, "From Lead Halide Perovskites to Lead-Free Metal Halide Perovskites and Perovskite Derivatives," *Advanced Materials*, vol. 31, no. 47. Wiley-VCH Verlag, Nov. 01, 2019. doi: 10.1002/adma.201803792.

[12] C. N. R. Rao, "Perovskites," 2001.

[13] F. F. Targhi, Y. S. Jalili, and F. Kanjouri, "MAPbI3 and FAPbI3 perovskites as solar cells: Case study on structural, electrical and optical properties," *Results Phys*, vol. 10, pp. 616–627, Sep. 2018, doi: 10.1016/j.rinp.2018.07.007.

[14] Y. Wei, Z. Cheng, and J. Lin, "An overview on enhancing the stability of lead halide perovskite quantum dots and their applications in phosphor-converted LEDs," *Chem Soc Rev*, vol. 48, no. 1, pp. 310–350, 2019, doi: 10.1039/C8CS00740C.

[15] C. Li, X. Lu, W. Ding, L. Feng, Y. Gao, and Z. Guo, "Formability of ABX 3 (X = F, Cl, Br, I) halide perovskites," *Acta Crystallogr B*, vol. 64, no. 6, pp. 702–707, 2008, doi: 10.1107/S0108768108032734.

[16] C. Li, X. Lu, W. Ding, L. Feng, Y. Gao, and Z. Guo, "Formability of ABX_3 (X = F, Cl, Br, I) halide perovskites," *Acta Crystallogr B*, vol. 64, no. 6, pp. 702–707, Dec. 2008, doi: 10.1107/S0108768108032734.

[17] M. Sessolo and H. J. Bolink, "Hovering solar cells," *Nat Mater*, vol. 14, no. 10, pp. 964–966, Oct. 2015, doi: 10.1038/nmat4405.

[18] S. D. Stranks *et al.*, "Electron-Hole Diffusion Lengths Exceeding 1 Micrometer in an Organometal Trihalide Perovskite Absorber," *Science (1979)*, vol. 342, no. 6156, pp. 341–344, Oct. 2013, doi: 10.1126/science.1243982.

[19] A. Miyata *et al.*, "Direct measurement of the exciton binding energy and effective masses for charge carriers in organic–inorganic tri-halide perovskites," *Nat Phys*, vol. 11, no. 7, pp. 582–587, Jul. 2015, doi: 10.1038/nphys3357.

[20] L. K. Ono, E. J. Juarez-Perez, and Y. Qi, "Progress on Perovskite Materials and Solar Cells with Mixed Cations and Halide Anions," *ACS Applied Materials and Interfaces*, vol. 9, no. 36. American Chemical Society, pp. 30197–30246, Sep. 13, 2017. doi: 10.1021/acsami.7b06001.

[21] W. J. Yin, T. Shi, and Y. Yan, "Unique properties of halide perovskites as possible origins of the superior solar cell performance," *Advanced Materials*, vol. 26, no. 27, pp. 4653–4658, Jul. 2014, doi: 10.1002/adma.201306281.

[22] M. M. Lee, J. Teuscher, T. Miyasaka, T. N. Murakami, and H. J. Snaith, "Efficient hybrid solar cells based on meso-superstructured organometal halide perovskites," *Science (1979)*, vol. 338, no. 6107, pp. 643–647, Nov. 2012, doi: 10.1126/science.1228604.

[23] M. A. Green, A. Ho-Baillie, and H. J. Snaith, "The emergence of perovskite solar cells," *Nature Photonics*, vol. 8, no. 7. Nature Publishing Group, pp. 506–514, 2014. doi: 10.1038/nphoton.2014.134.

[24] M. F. Mohamad Noh *et al.*, "The architecture of the electron transport layer for a perovskite solar cell," *Journal of Materials Chemistry C*, vol. 6, no. 4. Royal Society of Chemistry, pp. 682–712, 2018. doi: 10.1039/c7tc04649a.

[25] H. S. Jung and N. G. Park, "Perovskite solar cells: From materials to devices," *Small*, vol. 11, no. 1. Wiley-VCH Verlag, pp. 10–25, Jan. 07, 2015. doi: 10.1002/smll.201402767.

[26] C. Momblona *et al.*, "Efficient vacuum deposited p-i-n and n-i-p perovskite solar cells employing doped charge transport layers," *Energy Environ Sci*, vol. 9, no. 11, pp. 3456–3463, Nov. 2016, doi: 10.1039/c6ee02100j.

[27] Q. Wali, Y. Iqbal, B. Pal, A. Lowe, and R. Jose, "Tin oxide as an emerging electron transport medium in perovskite solar cells," *Solar Energy Materials and Solar Cells*, vol. 179, pp. 102–117, Jun. 2018, doi: 10.1016/j.solmat.2018.02.007.

[28] M. Dkhili *et al.*, "Attributes of High-Performance Electron Transport Layers for Perovskite Solar Cells on Flexible PET versus on Glass," *ACS Appl Energy Mater*, vol. 5, no. 4, pp. 4096–4107, Apr. 2022, doi: 10.1021/acsaem.1c03311.

[29] D. Prochowicz *et al.*, "Suppressing recombination in perovskite solar cells via surface engineering of TiO2 ETL," *Solar Energy*, vol. 197, pp. 50–57, Feb. 2020, doi: 10.1016/j.solener.2019.12.070.

[30] M. I. Ahmed, A. Habib, and S. S. Javaid, "Perovskite Solar Cells: Potentials, Challenges, and Opportunities," *International Journal of Photoenergy*, vol. 2015. Hindawi Limited, 2015. doi: 10.1155/2015/592308.

[31] G. V. Sannino *et al.*, "Development of SnO2 Composites as Electron Transport Layer in Unencapsulated CH3NH3PbI3 Solar Cells," *Solids*, vol. 2, no. 4, pp. 407–419, Dec. 2021, doi: 10.3390/solids2040026.

[32] Q. Jiang, X. Zhang, and J. You, "SnO2: A Wonderful Electron Transport Layer for Perovskite Solar Cells," *Small*, vol. 14, no. 31. Wiley-VCH Verlag, Aug. 02, 2018. doi: 10.1002/smll.201801154.

[33] R. L. Z. Hoye, K. P. Musselman, and J. L. MacManus-Driscoll, "Research Update: Doping ZnO and TiO2 for solar cells," *APL Mater*, vol. 1, no. 6, Dec. 2013, doi: 10.1063/1.4833475.

[34] G. Yang *et al.*, "Embedding SnO2Thin Shell Protected Ag Nanowires in SnO2ETL to Enhance the Performance of Perovskite Solar Cells," *Langmuir*, vol. 38, no. 21, pp. 6752–6760, May 2022, doi: 10.1021/acs.langmuir.2c00792.

[35] L. Xiong *et al.*, "Review on the Application of SnO2 in Perovskite Solar Cells," *Advanced Functional Materials*, vol. 28, no. 35. Wiley-VCH Verlag, Aug. 29, 2018. doi: 10.1002/adfm.201802757.

[36] F. Rezwana Chowdhury, S. Choudhury, F. Hasan, and T. Begum, "OPTICAL PROPERTIES OF UN-DOPED AND INDIUM-DOPED TIN OXIDE THIN FILMS," 2011.

[37] J. Song *et al.*, "Lowerature SnO2-based electron selective contact for efficient and stable perovskite solar cells," *J Mater Chem A Mater*, vol. 3, no. 20, pp. 10837–10844, May 2015, doi: 10.1039/c5ta01207d.

[38] K. Deng, Q. Chen, and L. Li, "Modification Engineering in SnO2 Electron Transport Layer toward Perovskite Solar Cells: Efficiency and Stability," *Advanced Functional Materials*, vol. 30, no. 46. Wiley-VCH Verlag, Nov. 01, 2020. doi: 10.1002/adfm.202004209.

[39] R. S. Lanigan, T. A. Yamarik, and F. A. Andersen, "Final report on the safety assessment of EDTA, calcium disodium EDTA, diammonium EDTA, dipotassium EDTA, disodium EDTA, TEA-EDTA, tetrasodium EDTA, tripotassium EDTA, trisodium EDTA, HEDTA, and trisodium HEDTA," *International Journal of Toxicology*, vol. 21, no. SUPPL. 2. pp. 95–142, Sep. 2002. doi: 10.1080/10915810290096522.

[40] D. Yang *et al.*, "High efficiency planar-type perovskite solar cells with negligible hysteresis using EDTA-complexed SnO2," *Nat Commun*, vol. 9, no. 1, Dec. 2018, doi: 10.1038/s41467-018-05760-x.

[41] H. Choi, J. H. Song, J. Jang, X. D. Mai, S. Kim, and S. Jeong, "High performance of PbSe/PbS core/shell quantum dot heterojunction solar cells: short circuit current enhancement without the loss of open circuit voltage by shell thickness control," *Nanoscale*, vol. 7, no. 41, pp. 17473–17481, 2015, doi: 10.1039/C5NR03309H.

[42] S. Y. Park and K. Zhu, "Advances in SnO2 for Efficient and Stable n–i–p Perovskite Solar Cells," *Advanced Materials*, vol. 34, no. 27. John Wiley and Sons Inc, Jul. 01, 2022. doi: 10.1002/adma.202110438.

[43] A. R. Razeghizadeh, I. Kazeminezhad, L. Zalaghi, and V. Rafee, "Effects of Sol concentration on the structural and optical properties of SnO 2 Nanoparticle."

[44] W. Long, A. He, S. Xie, X. Yang, and L. Wu, "Prospect of SnO2 Electron Transport Layer Deposited by Ultrasonic Spraying," *Energies (Basel)*, vol. 15, no. 9, May 2022, doi: 10.3390/en15093211.

[45] K. Derrar, M. Zaabat, I. Zerrouk, A. Hafdallah, N. Rouabah, and B. Gasmi, "Optical and structural properties of sno2 thin films deposited by spray pyrolysis technique: Effect of solution concentration," *Defect and Diffusion Forum*, vol. 397, pp. 179–186, 2019, doi: 10.4028/www.scientific.net/DDF.397.179.

[46] A. M. A. Leguy *et al.*, "Experimental and theoretical optical properties of methylammonium lead halide perovskites," *Nanoscale*, vol. 8, no. 12, pp. 6317–6327, 2016, doi: 10.1039/C5NR05435D.

[47] N. Balagowtham, K. R. Acchutharaman, N. Santhosh, M. S. Pandian, and P. Ramasamy, "Highly stable MAPbI3 microcrystals: a single precursor derived from low-grade PbI2 using sono-chemical method for economical and efficient perovskite solar cells," *Journal of Materials Science: Materials in Electronics*, vol. 33, no. 27, pp. 21531–21545, Sep. 2022, doi: 10.1007/s10854-022-08944-w.

[48] Q. Chen *et al.*, "Controllable Self-Induced Passivation of Hybrid Lead Iodide Perovskites toward High Performance Solar Cells," *Nano Lett*, vol. 14, no. 7, pp. 4158–4163, Jul. 2014, doi: 10.1021/nl501838y.

[49] Z. Chu *et al.*, "Impact of grain boundaries on efficiency and stability of organic-inorganic trihalide perovskites," *Nat Commun*, vol. 8, no. 1, p. 2230, Dec. 2017, doi: 10.1038/s41467-017-02331-4.

[50] M. Zhu, Z. Sun, M. Fujitsuka, and T. Majima, "Z-Scheme Photocatalytic Water Splitting on a 2D Heterostructure of Black Phosphorus/Bismuth Vanadate Using Visible Light," *Angewandte Chemie International Edition*, vol. 57, no. 8, pp. 2160–2164, Feb. 2018, doi: 10.1002/anie.201711357.

[51] E. Khorshidi *et al.*, "Hydrophobic Graphene Quantum Dots for Defect Passivation and Enhanced Moisture Stability of CH 3 NH 3 PbI 3 Perovskite Solar Cells," *Solar RRL*, vol. 6, no. 7, Jul. 2022, doi: 10.1002/solr.202200023.

[52] B. Zhang *et al.*, "Heterojunction *In Situ* Constructed by a Novel Amino Acid-Based Organic Spacer for Efficient and Stable Perovskite Solar Cells," *ACS Appl Mater Interfaces*, vol. 14, no. 36, pp. 40902–40912, Sep. 2022, doi: 10.1021/acsami.2c09926.

[53] S. Panigrahi *et al.*, "Tailoring the Interface in High Performance Planar Perovskite Solar Cell by ZnOS Thin Film," *ACS Appl Energy Mater*, vol. 5, no. 5, pp. 5680–5690, May 2022, doi: 10.1021/acsaem.1c04064.

A

AN APPENDIX

A.1 Solar cell parameters

In this section, the calculation of the solar cell's parameters (Figure 41) are explained with the aid of the IV and PV curves obtained in the chapter Results and Discussion and using the key equations to extract its values.
Figure 41 - Representation of a general IV curve along with the solar cell parameters

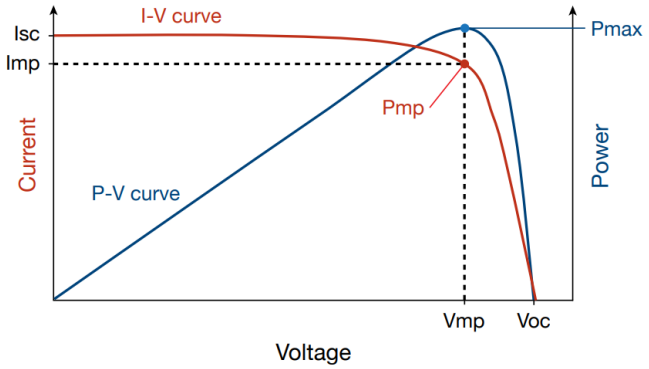

Figure 41 - Representation of a general IV curve along with the solar cell parameters.

The solar cell parameters can be calculated in the following way:

- I_{SC} (short circuit current) is the current value at V = 0 V.
- V_{OC} (open circuit voltage) is the voltage value at I = 0 A.
- I_{mp} and V_{mp} are the values of current and voltage, respectively, at which the power reaches its maximum value and can be obtained by analyzing the IV curve.
- P_{max} (maximum power) can be obtained using the following equation:

$$P_{max} = I_{mp} \times V_{mp}$$

- FF (fill factor) is the approximation of the IV curve to a square and can be calculated through the following equation:

$$FF = \frac{I_{mp} \times V_{mp}}{I_{SC} \times V_{OC}}$$

- PCE (power conversion efficiency) is the ratio between P_{max} and P_{light} (1 kW/m^2):

$$PCE = \frac{P_{max}}{P_{light}} \times 100\%$$

Rs (series resistance) and Rsh (shunt resistance) can be obtained by calculating the inverse slope of the IV curve in the areas shown in Figure 42. In the ideal scenario, these two parameters have the values: Rs≈0 and Rsh≈∞.

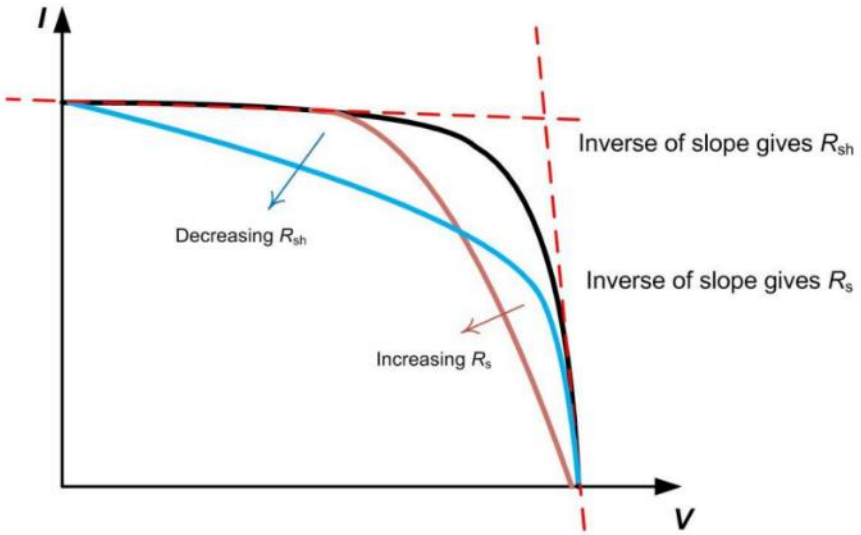

Figure 42 - Effect of the decrease of shunt resistance (blue) and increase of series resistance (red) on the IV curve of a solar cell [55].

A.2 Materials

Table 3 - List of materials used in this work, and their abbreviation, purity value, CAS number and company.

Material	Abbreviation	Purity	CAS number	Company
Chlorobenzene	-	99.9%	108-90-7	SIGMA ALDRICH
Dimethyl sulfoxide	DMSO	99.9 %	67-68-5	Fisher Chemical
Ethylenediamine tetraacetic acid	EDTA			
Lead iodide	PbI2	99%	10101-63-0	SIGMA ALDRICH
Lithium salt	Li-TFSI	99.95%	90076-65-6	SIGMA ALDRICH
Methylammonium iodide	MAI	98%	14965-49-2	SIGMA ALDRICH
N-n dimethylformamide	DMF	99.8 %	68-12-2	Panreac
Tin oxide (IV), 15% colloidal solution	SnO_2	15%	18282-10-5	Alfa Aesar
4-TERT-BUTYLPYRIDINE		98%	3978-81-2	SIGMA ALDRICH
SPIRO-OMETAD		99.5%	207739-72-8	Ossila

A.3 Solutions preparation

1. ETL

The SnO_2 solutions were prepared by diluting the SnO_2 aqueous colloidal solution (15 wt%) with de-ionized water to achieve the desired concentration and then stirred for 2 hours at room temperature. The desired concentrations were obtained by using the following quantities:

- 15 wt% SnO_2: No need for dilution. The solution used was the same from the bottle.

- 10 wt% SnO_2: 1 mL SnO_2 (15 wt%) + 0.5 mL deionized water.
- 7.5 wt% SnO_2: 1 mL SnO_2 (15 wt%) + 1 mL deionized water.
- 2.5 wt% SnO_2: 1 mL SnO_2 (15 wt%) + 5 mL deionized water.

The E-SnO2 solutions were prepared by mixing with a volume ratio of 1:1 the solutions of SnO2 previously prepared with an EDTA solution followed by a 5h stirring process on a hotplate at 80 °C. The EDTA solution was prepared by mixing 0.2 mg of EDTA with 1 mL of deionized water and stirring for 2h at room temperature. The desired concentrations were obtained using the following quantities:

- 15 wt% E-SnO_2: 1 mL SnO_2 (15 wt%) + 1mL deionized water
- 10 wt% E-SnO_2: 1 mL SnO_2 (10 wt%) + 1 mL deionized water.
- 7.5 wt% E-SnO_2: 1 mL SnO_2 (7.5 wt%) + 1 mL deionized water.
- 2.5 wt% E-SnO_2: 1 mL SnO_2 (2.5 wt%) + 1 mL deionized water.

2. Perovskite precursor solution

The perovskite solution was obtained by dissolving 622 mg of lead iodide (PbI_2) in a solution with 750 µL of N-N dimethylformamide (DMF) and 95 µL of dimethylsulfoxide (DMSO). After the PbI_2 was fully dissolved, 215 mg of methylammonium iodide (MAI) were added to the solution and it was left stirring overnight at room temperature. Before the deposition, the perovskite solution was filtered using PTFE filters with a 0.25 µm grading.

3. HTL precursor solution

The HTL solution was prepared by mixing 27.1 mg of Spiro-OMETAD, 6.56 µL of LiTFSI, 10.685 µL of 4-tert-butylpyridine and 375 µL of chlorobenzene. The LiTFSI solution was made by mixing 20.8 mg of Lithium Salt with 40 µL of acetonitrile. The HTL solution was then stirred for 3 hours at room temperature.

A.4 Optical characterization

In this appendix, optical characterizations of the ETL and $MAPbI_3$ films are presented.

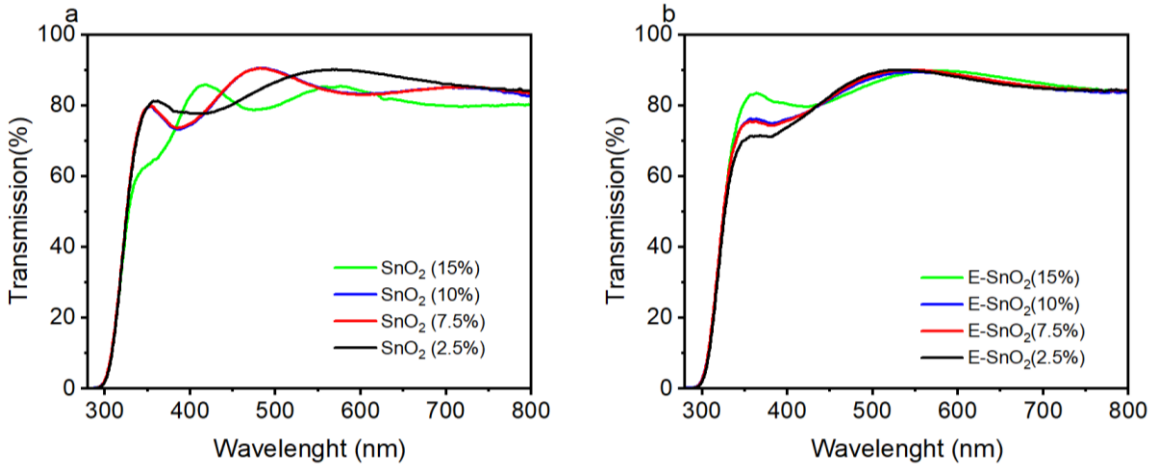

Figure 43 -Transmission spectra of a) SnO_2 and b) E-SnO_2 with different concentrations.

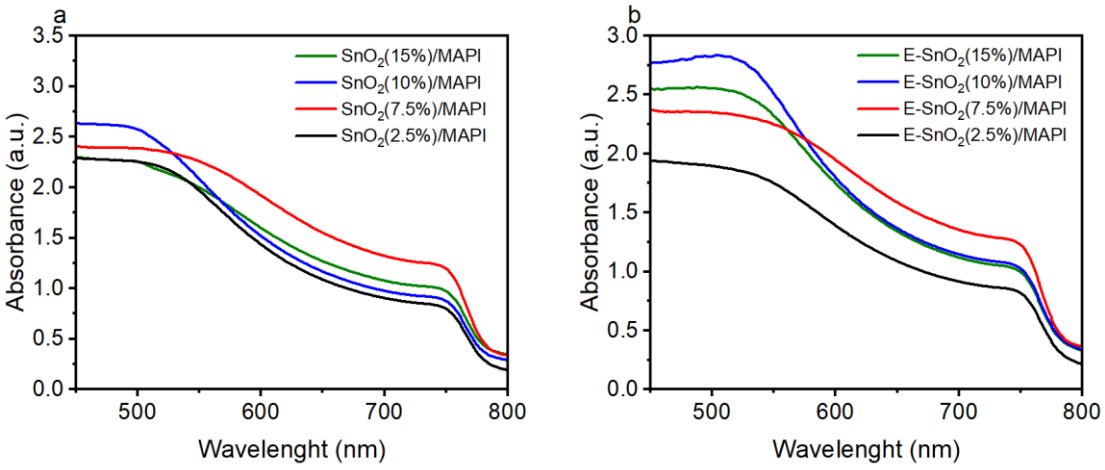

Figure 44 - Absorbance spectra of $MAPbI_3$ films deposited on a) SnO_2 and b) E-SnO_2 with different concentrations.

A.5 Structural characterization

In this appendix, structural and morphological characterizations of the ETL and $MAPbI_3$ films are presented.

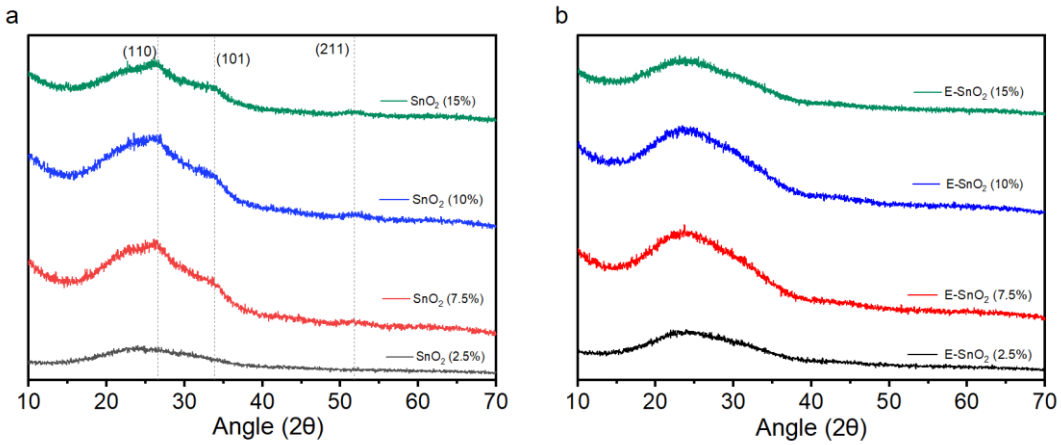

Figure 45 – XRD plot of a) SnO_2 and b) E-SnO_2 with different concentrations.

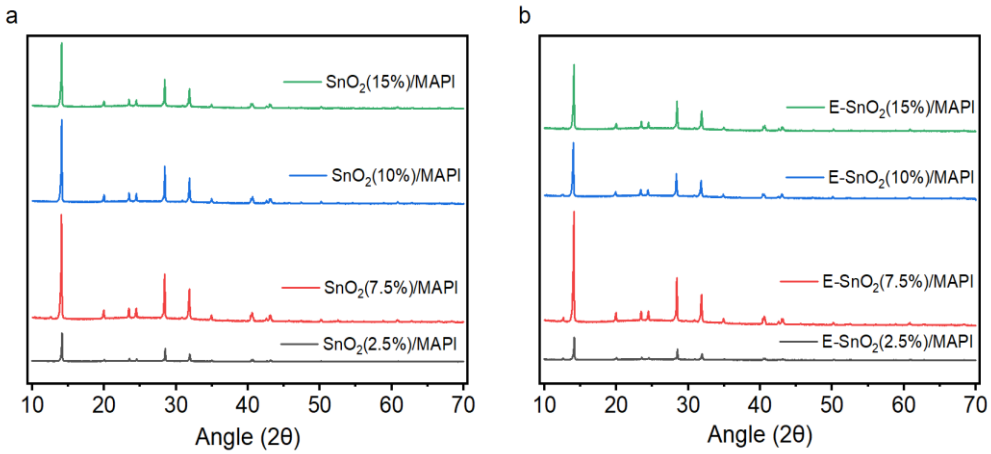

Figure 46 - XRD plot of $MAPbI_3$ film deposited on a) SnO_2 and b) E-SnO_2 with different concentrations.

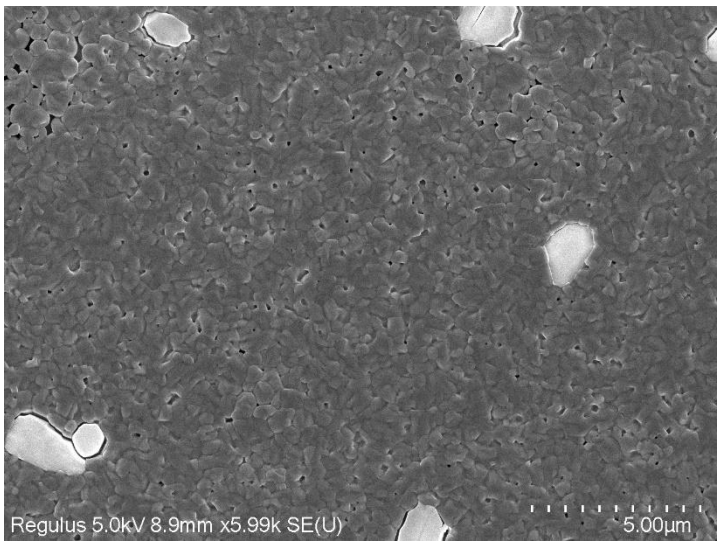

Figure 47 - SEM image of a $MAPbI_3$ film deposited on E-SnO_2 with 7.5% concentration.

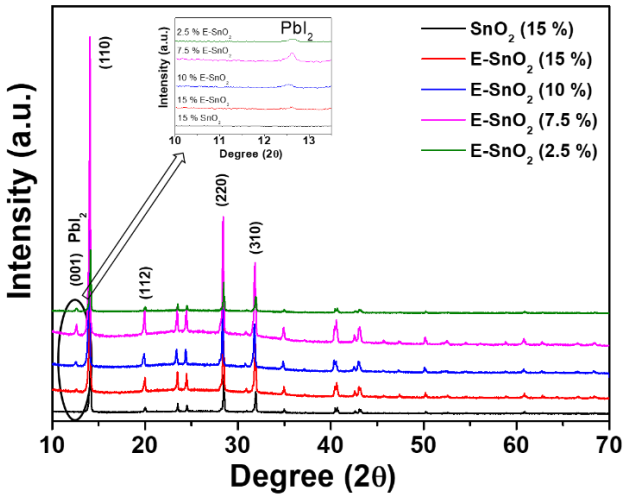

Figure 48 - XRD plot of MAPbI3 film deposited on SnO_2 with 15% concentration and E-SnO_2 with different concentrations.

NOVA SCHOOL OF SCIENCE & TECHNOLOGY

A VERY LONG AND IMPRESSIVE THESIS TITLE WITH A FORCED LINE BREAK

JOHN DOE

⟨year⟩

A VERY LONG AND IMPRESSIVE THESIS TITLE
WITH A FORCED LINE BREAK

JOHN VERY LONGNAME DOE

⟨year⟩